Quantitative MRI of the carotid artery:

Simultaneous T_1 and T_2 mapping on complex image data using maximum likelihood parameter estimation

K.M. van Hespen

Technische Universiteit Delft

TU Delft Delft University of Technology

Challenge the future

Quantitative MRI of the carotid artery: Simultaneous T_1 and T_2 mapping on complex image data using maximum likelihood parameter estimation

performed at Erasmus MC

by

Kees van Hespen

to obtain the degree of Master of Science
at the Delft University of Technology,
to be defended publicly on 28 September 2016

Student number:	4064062
Project duration:	September 1, 2015 – May 31, 2016
Supervisors:	Dr. Ir. D.H.J. Poot,
	Dr. Ir. S. Klein,
	Dr. Ir. H.A. Nieuwstadt

TU Delft Delft University of Technology

Acknowledgments

I would like to take this moment to thank a few people that helped me accomplish my work. After a solid nine months I assembled my final chapter as a student, which could not have been done without several people. I would like to thank Dr. Dirk Poot and Dr. Stefan Klein for their daily support. They coped with the abundant amount of questions I had on maximum likelihood estimation and image registration. I learned a lot during my thesis period and I couldn't have wished for better supervision. I would also like to thank Dr. Harm Nieuwstadt (★29 April 1985 - †3 May 2016), for helping me find my place in the EMC and helping me to start up my project.

I would also like to thank my friends and colleagues from the EMC. You were a great inspiration for new ideas for my thesis and a way to escape the thesis project for a while, by talking about non-scientific subjects, save for the discussions on Tesla here and there.

My thanks also go to my family and my girlfriend, who took care of the emotional support for my project and believing in my capacities whenever I failed to see them.

Thanks for everything.

Kees van Hespen

Contents

1

Introduction

The number of people that experienced a stroke in 2010 in the US is estimated to be 795.000 [1]. Strokes are the cause of roughly 140.000 deaths annually. 87% of these strokes are caused by an ischemic event [2]. Carotid atherosclerotic plaque rupture contributes to 15-20% of all ischemic strokes [3]. Carotid atherosclerotic plaque is the result of an inflammation in the carotid vessel wall, which gets progressively worse [4, 5]. Vulnerable atherosclerotic plaque can rupture, and the expelled contents can become thrombotic material. When this thrombotic material gets stuck in a cerebral artery, an ischemic event results. The luminal narrowing caused by the growing of the plaque, called stenosis, has commonly been used for identification of plaque severity [6]. There have been signs that plaque composition is also important in identification of plaque severity [7]. Intraplaque hemorrhages (IPH) and calcifications have shown to be a risk factor in plaque vulnerability [3, 8, 9]. Non invasive methods for the analysis of plaque composition are therefore required (see Appendix A).

Magnetic resonance imaging (MRI) can characterize plaque composition based on magnetic resonance tissue properties [10, 11]. Two of these tissue properties, called T_1 and T_2, are magnetic relaxation times. Each tissue has a T_1-T_2 combination, enabling characterization of tissue type by their relaxation times [12, 13]. In clinical practice, T_1 and T_2 weighted images are usually acquired. Contrast is obtained between tissues in these weighted images, due to signal intensity differences caused by differences in relaxation times. However, T_1 and T_2 weighted images acquired using different pulse se-

quences or brands of scanners, can yield different intensity values for similar tissues across multiple images. Even the repositioning of the radiofrequency surface coils on the same patient and scanner can induce apparent contrast differences between tissues. This makes the comparison of images, using only the voxel intensity values, difficult, especially for automatic segmentation methods. Quantitative MRI aims at measuring quantitative values, T_1 and T_2, as opposed to generating visually pleasing images optimized for qualitative analysis. With quantitative MRI we can potentially produce the same results regardless of the type of MR scanner or the positioning of the radio-frequency neck coil. By mapping T_1 and T_2 instead of the MR signal, we can compare measurements between and within patients. This would be highly beneficial for accurate assessment of carotid plaque composition.

The estimation of T_1 and T_2 is performed by fitting a mathematical model to a set of T_1 and T_2 weighted images. The MR scanner can employ several pulse sequences that can produce T_1 and T_2 weighted images. Such acquisition methods include Variable Flip angle (VFA), Look Locker (LL) and Inversion recovery (IR) [14–16] that induce a T_1 weighting in the image, and T_2 weighting methods such as Fast spin echo (FSE) and gradient-and spin echo (GRASE) [17, 18]. Each method has its advantages and disadvantages regarding time efficiency and accuracy. IR only induces a T_1 weighted effect, whereas VFA and LL also induce a T_2 weighted effect in the image. On the other hand, IR images take relatively longer to acquire than VFA and LL images, which could potentially induce errors or motion artifacts in the image.

We aim to produce T_1 and T_2 maps of the carotid artery wall in a short amount of time. To this end, an optimized acquisition method was developed in previous work. The acquisition method uses three pulse sequences, giving a T_1 or T_2 weighting of the signal, namely: spin echo, inversion recovery and saturation recovery. In this acquisition, the number of images from which T_1 and T_2 can be fitted is very low, which imposes challenges in T_1 and T_2 fitting.

Currently, most methods estimate the parameters T_1 and T_2 by fitting a mathematical model to a series of acquired magnitude MR images [14, 19–22], see Appendix A. Intrinsically, MR data is complex of nature. When the magnitude data is used, phase information is removed. For T_1 estimation using multiple T_1 weighted images, the loss of phase data is not a problem, since there are enough measurements to correctly fit the signal model. In our

acquisition scheme, where the number of acquired images is low, sign removal by discarding the phase data, may be problematic as will be shown in Section 2.4. In this case, ambiguous T_1 and T_2 estimates could potentially be found, which hampers reproducibility and accuracy of the maps [23]. A second disadvantage of using the magnitude signal is the Rician distribution of the data. The non zero mean of this distribution may result in a bias in the estimated T_1 and T_2 [24, 25]. A potential disadvantage of using complex data is the possible introduction of phase errors [26], see Appendix A.

Another source of inaccuracy in T_1 and T_2 estimation is due to translation between images. The parameter estimation method assumes that each voxel represents the same anatomical structure in each image [27, 28]. Due to translation of the subject, this assumption is not necessarily true, and T_1 and T_2 estimation becomes incorrect for misaligned voxels [29]. For this purpose image registration is needed, which aligns the images. Misalignment of the images can have a significant impact on the reproducibility of T_1 and T_2, since the carotid wall is only several voxels wide. Research of other groups that use registration to compensate for translation can be found in Appendix A.

In this thesis we will try to solve the challenges posed by the used acquisition scheme, in the estimation of T_1 and T_2. In order to do so, we will investigate the use of complex data. To use complex data, a signal model needs to be defined that can represent the complex MR signal, which will be discussed in Section 2.4. The feasibility of this model will be evaluated on simulated data and data acquired from a hardware phantom. With the hardware phantom data we can evaluate the presence and/or influence of phase errors, due to the use of complex data. We will also focus on image registration, and how it impacts the reproducibility of the estimated parameters. Three different registration methods will be explored that can potentially increase the reproducibility of the estimated parameters due to better alignment of the images, see Section 2.3. To evaluate the registration methods, we use data acquired from healthy volunteers. Each volunteer was scanned twice, which allows us to evaluate the reproducibility by comparing the T_1 and T_2 maps between scan and rescan, and between volunteers.

2

Methods

The estimation of T_1 and T_2 from acquired images can be visualized with a processing pipeline, given in Figure 1. This pipeline can be split up in four parts: image acquisition (the acquisition of MR data), image reconstruction (the reconstruction of MR data to spatial images), image registration (the alignment of images), and mapping (the estimation of T_1 and T_2). Image acquisition and image reconstruction have been optimized in previous studies. And as discussed in the introduction, image registration and mapping will be evaluated in this thesis. In the following subsections we will elaborate on each of the four parts of the pipeline.

2.1 Acquisition

For quantitative assessment of the carotid plaque components, MR images were acquired. A subject is placed in an MRI scanner and on both the left and right side of the neck, a radiofrequency surface neck coil with two

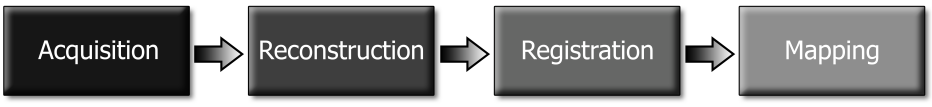

Figure 1: Visualization of the processing pipeline where MR images are acquired and T_1 and T_2 maps are produced

channels each, is placed. The pulse sequence that is hereafter played out by the scanner consists of two modules: a preparation module, that induces T_1 or T_2 weighting, and a readout module that was used to acquire the MR signal. Three preparation modules were used for our images, namely a spin echo preparation, saturation preparation and inversion preparation. These preparation modules and the readout module will be discussed in the following subsections.

2.1.1 CUBE sequence

A 3D CUBE readout module was used for each preparation module. CUBE consists of FSE with varying flip angles [30]. Conventionally FSE uses fixed flip angles [31]. In FSE a 90 degree radiofrequency (RF) pulse is applied to the spins, given in Figure 2.A. Due to inhomogeneities in the magnetic field, the spins start to dephase, and the signal strength decreases rapidly with a time constant T_2^*, Figure 2.B. At half the spin echo time, T_E, a 180 degree pulse is applied, Figure 2.C. This places the slower running spins ahead of the faster running spins. At time T_E, the faster running spins have caught up with the slower running spins, and an echo signal is produced. For time efficiency, multiple echos were acquired after one 90 degree flip.

Due to T_2 relaxation, the echo signal decreases over time. In order to keep the SNR constant over multiple echos, the fixed 180 degree flip angles can be replaced by variable flip angles. By doing so, the magnetization is flipped partially in the longitudinal direction. By storing a part of the magnetization in an encoded longitudinal state, the magnetization can be converted back to transversal magnetization at a later echo, keeping the echo signal constant over multiple echoes [30].

2.1.2 Spin echo preparation

A spin echo (SE) preparation was used to induce a combination of T_1 and T_2 weighting in the image. A 90 degree pulse flips the longitudinal magnetization (M_z) into the transversal plane, see Figure 3. The transversal magnetization M_{xy}, starts to decay with a time constant T_2. For refocusing of T_2^* weighted effects, a 180 degree pulse was applied. At T_E, an echo signal is produced, and the signal is brought back into the longitudinal plane with another 90 degree pulse. Subsequently, the CUBE readout sequence was played out that acquires the recovered MR signal. And after a repetition time T_R, the sequence was repeated.

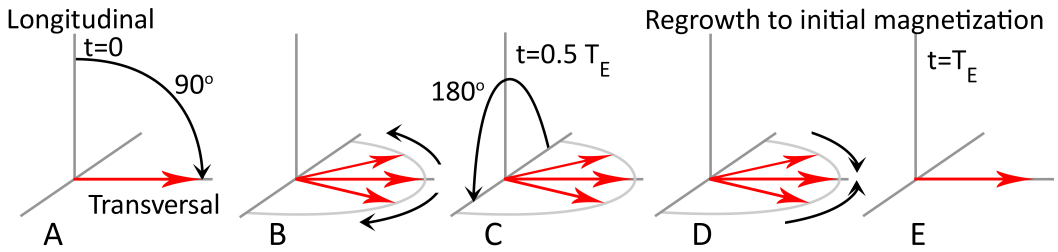

Figure 2: Spin echo. A: Initial magnetization after 90 degree flip. B: Spin dephasing. C: 180 degree flip. D: Spin rephasing. E: Echo signal

The equation that describes the evolution of the signal for this preparation is modeled by [32]:

$$S = A(1 - e^{-(T_R - T_E)R_1})e^{-T_E R_2} \tag{1}$$

, given $T_1 \gg T_E$, where A is the unprepared magnetization, T_R the repetition time, T_E the echo time and, R_1 is $1/T_1$ and R_2 is $1/T_2$, the tissue specific properties.

2.1.3 Saturation preparation

Saturation (SR) preparation comprises of two 90 degree pulses. The initial magnetization, just before the first 90 degree pulse in Figure 4, is flipped in the transversal plane with a 90 degree pulse. Over time, the longitudinal magnetization will recover with a time constant T_1, and the transversal magnetization will decrease with a time constant T_2 due to the absence of an RF field. After a time T_R a subsequent 90 degree is applied. The already recovered magnetization, is flipped into the transversal plane again where it can be read out. The signal intensity after the first 90 degree pulse can be modeled by:

$$S = A(1 - e^{-T_R R_1}) \tag{2}$$

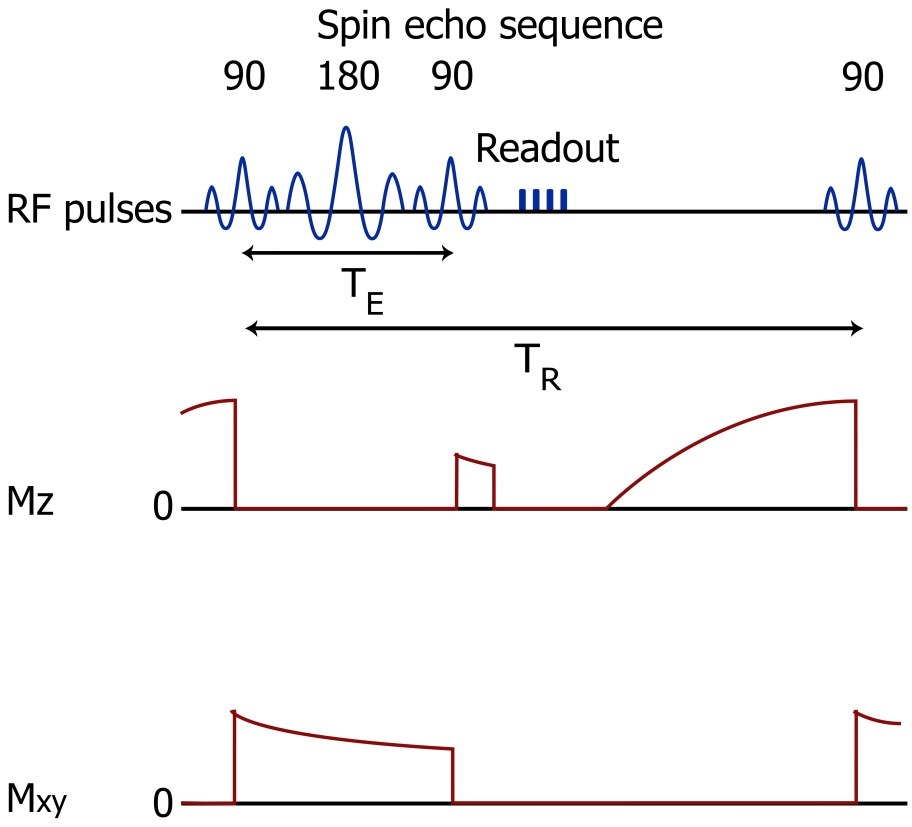

Figure 3: Pulse diagram, longitudinal and transversal magnetization for a spin echo preparation

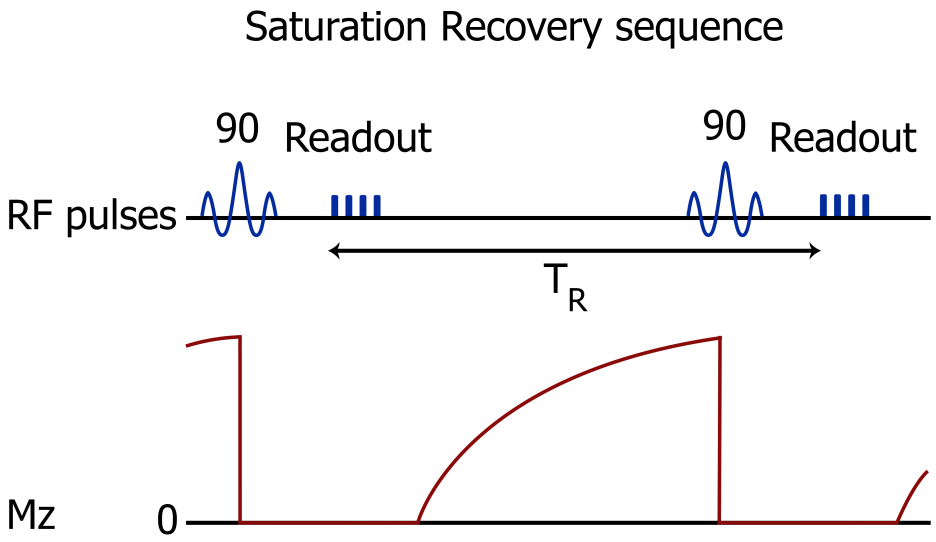

Figure 4: Pulse diagram and longitudinal magnetization for saturation preparation

2.1.4 Inversion preparation

An inversion (IR) preparation consists of two RF pulses. Ideally, the first pulse flips the magnetization with 180 degrees, inverting the orientation of the spins. When a non-adiabatic pulse is used, inhomogeneities in the RF field may impact the applied flip angle, and flip a portion of the longitudinal magnetization in the transversal plane [33]. Therefore, adiabatic pulses were used, that do not suffer from inhomogeneities in the RF field and can uniformly flip the magnetization in a subject [34]. After the 180 degree pulse the longitudinal magnetization will recover, see Figure 5. After an inversion time T_I a 90 degree pulse is applied. This brings the recovered longitudinal magnetization in the transversal plane. In the transversal plane, the signal can be read out. The magnitude signal can be modeled by Equation 3, where B is the inversion efficiency, which models the efficiency of the 180 degree adiabatic inversion pulse. When a flip angle of 180 degrees is applied, $B = 2$. When no flip is applied, $B = 0$. In previous work it was concluded that $B = 1.95$ was appropriate for neck tissue.

$$S = |A(1 - Be^{-T_I R_1} + (B-1)e^{-T_R R_1})| \tag{3}$$

An advantage of IR is that in contrast to SR, the contrast range is larger

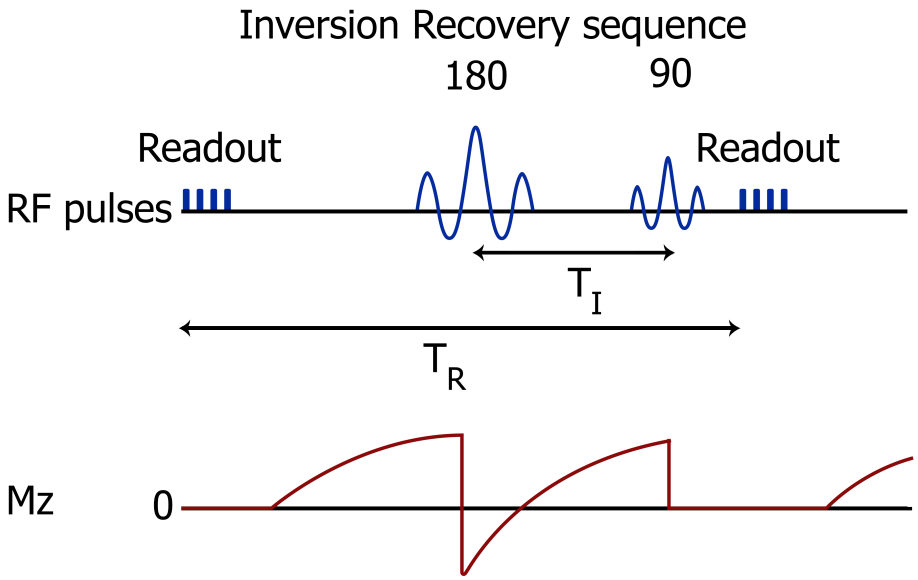

Figure 5: Pulse diagram and longitudinal magnetization for inversion preparation

when complex data is used [26]. Due to the fact that the magnetization is allowed to be negative, the M_z range goes from -M_0 to M_0, in comparison to 0 to M_0 for saturation prepared imaging. However, the addition of parameter B in the IR signal model, increases the complexity of parameter estimation.

2.1.5 Sequence settings

In preliminary work at Erasmus MC, the amount of images per preparation module and the preparation module settings were optimized for accuracy and time efficiency, i.e. T_1 and T_2 accuracy per unit of scan time. The acquisition scheme for T_1 weighting consists of two images with an IR preparation and two images with a SR preparation. For T_2 weighting, five images with a SE preparation were acquired. T_I, T_R and T_E for these preparations are given in Table 1.

As an example, images acquired with the settings described in Table 1 are given in Figure 6. In this figure there is a clear difference between the contrast in the SR images and the other images. The images that are given in this figure were reconstructed magnitude images, using the reconstruction as

Table 1: T_I, T_R and T_E in seconds, for the used preparation modules

Image nr.	**1**	**2**	**3**	**4**	**5**	**6**	**7**	**8**	**9**
Sequence	**IR**	**IR**	**SE**	**SE**	**SE**	**SE**	**SE**	**SR**	**SR**
$T_I(s)$	0.091	0.429	0	0	0	0	0	0	0
$T_E(s)$	0	0	0.028	0.03	0.032	0.033	0.034	0	0
$T_R(s)$	0.954	3.694	1.336	1.336	1.336	1.336	1.336	1.056	0.876

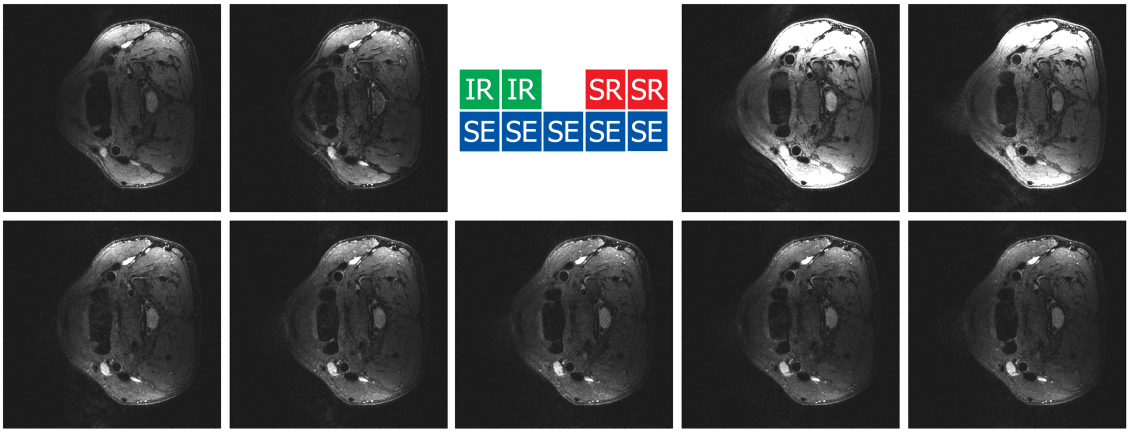

Figure 6: Magnitude images corresponding to the sequence settings described in Table 1

described in the next subsection.

2.2 Reconstruction

The acquired MR signal is stored in a Fourier space, called k-space. This k-space data needs to be reconstructed into image space. Normally the MRI scanner reconstructs this data into magnitude images, discarding information on the phase data. By reconstructing the images ourselves, using an already developed method, the complex nature of the data remains intact. In Figure 7, the real and imaginary part of a complex image are given as example.

For the reconstruction of the images, the complex valued coil sensitivity profiles of the neck coils were used. In Figure 8.A-D, the magnitude of the sensitivity maps is given for all channels and coils. The corresponding reconstructed image is given in Figure 8.E. The same sensitivity profile was used for the reconstruction of all images from the same scan session. If a different profile was used for each image, the noise in each reconstructed

image could be different, adding additional variability in the mapping results. Hence, the same complex valued coil sensitivity profiles were used for the reconstruction of all images.

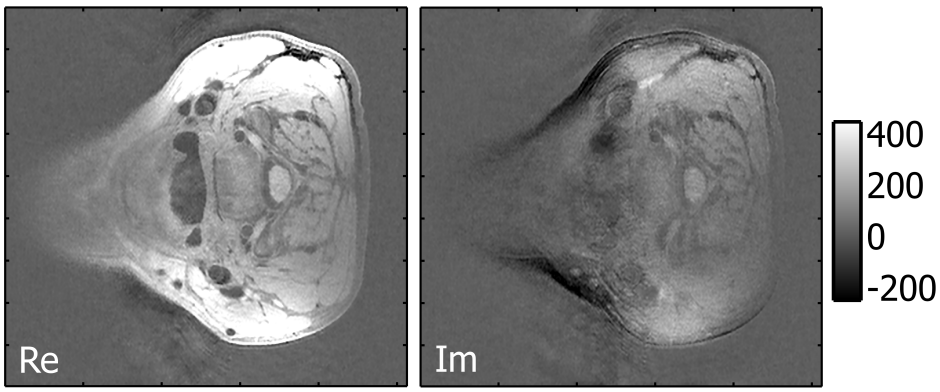

Figure 7: Real (Re) and imaginary (Im) parts of an MR image

2.3 Registration

During the acquisition of the T_1 and T_2 weighted images, translation of the subject can occur due to breathing, swallowing or repositioning of the head. This results in a misalignment between all images and hampers quantitative assessment, since in this case a given voxel does not represent the same anatomical structure in each image. To account for these effects, image registration can be applied. Registration can also be used in the evaluation of reproducibility, for baseline-follow up scan comparison.

Registration is the process in which an image, called the moving image, is deformed to fit another image, the fixed image, using the transformation $T(x)$ of the voxels x. The transformation describes how a moving image needs to be deformed to align with a fixed image, and is defined as the transformation from fixed to moving image domain, as the arrow in Figure 9 implies.

In Figure 9, the transformation T of the given data point describes the relation between the location of this point in the fixed and moving image, p and q. The transformation that is applied to align the fixed and moving

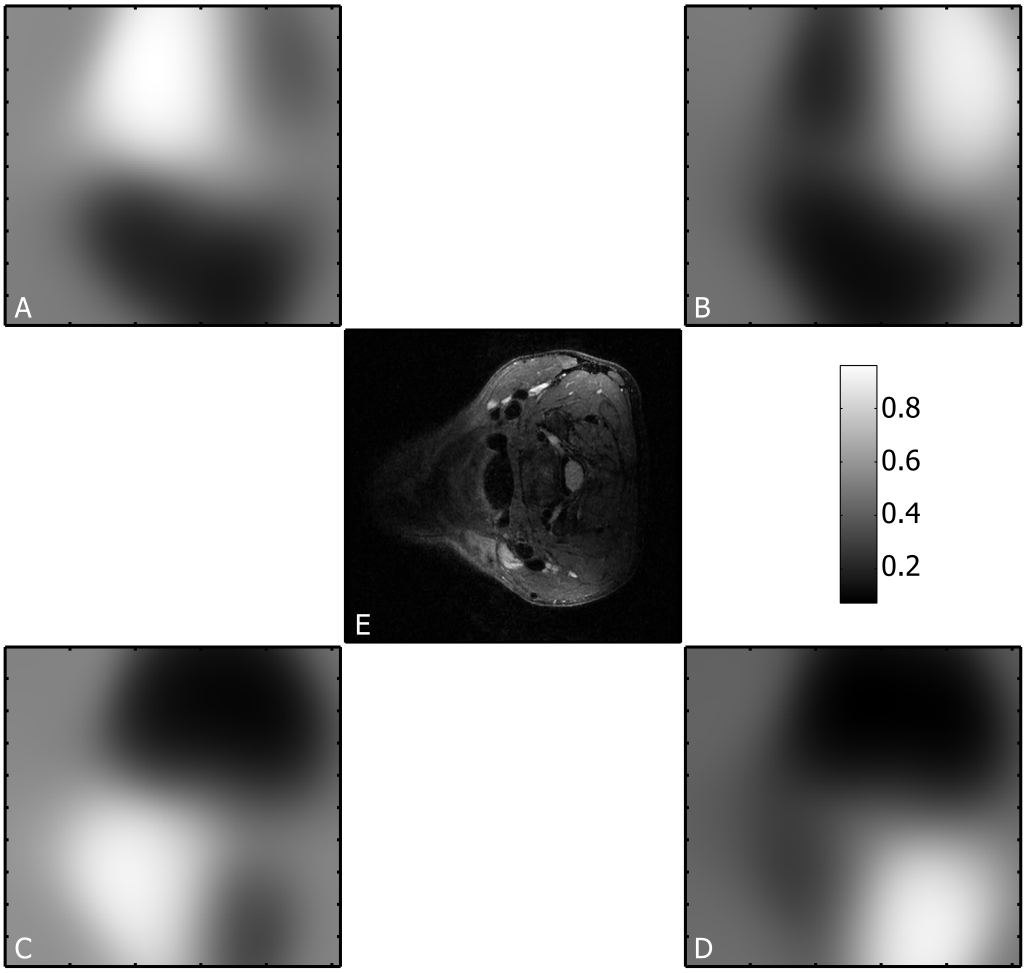

Figure 8: Coil sensitivity maps used in the reconstruction. A: Coil 1, channel 1, B: Coil 1, channel 2, C: Coil 2, channel 1, B: Coil 2, channel 2, E: Reconstructed image

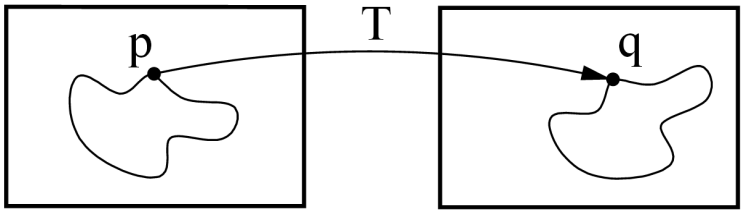

Figure 9: Pairwise registration of point p in one image to point q in another image [35]

images, can either be rigid or non rigid. A rigid transformation involves rotation and translation of the fixed image. A non rigid, affine transformation has no restrictions, e.g. it can translate, rotate, scale, deform and shear the image.

We propose three different registration methods, each performing registration between the images in a scan (intrascan registration) and registration between scans (interscan registration), for baseline-followup scan comparison. Pairwise, groupwise and multi pairwise registration, will be discussed in the following subsections.

2.3.1 Pairwise

In pairwise registration one moving image was registered to one fixed image. Pairwise registration is described by the optimization of the transformation parameters μ, given by:

$$\hat{\mu} = \arg\max_{\mu} \mathcal{S}(S_a^b(x), S_c^d(T_c(x))) \tag{4}$$

where $\mathcal{S}(S_a^b(x), S_c^d(T(x)))$ is the similarity metric that compares the fixed and moving image, where $S_a^b(x)$ is image a in scan session b, and $S_c^d(T_c(x))$ is the transformed image c in scan session d. The metric that was used is based on mutual information. Mutual information is a measure of the information contained in one image about another image, and depends on the joint probability distribution [36].

In Figure 10, pairwise registration for two scans is visualized, where the direction of registration is given by the arrows. For each scan, image 8 was used as fixed image, since this image had the highest contrast, see the SR images in Figure 6. The other images in the same scan were used as moving

images. For these moving images specific transformations were estimated, that transform the moving image to the fixed image.

Linking the inter- and intrascan transformation, we obtained images that are aligned between scan sessions but also maintain intrascan alignment. In the following examples $T_{S_b^a \to S_d^c}(x)$ gives the transformation that transforms the image points x from image b in scan a to image d in scan c. The voxel values of image 5 of scan 2, S_5^2 in Figure 10 can be transformed to S_8^1, by transforming S_8^1 to S_8^2 using transformation $T(x)$ of data points x in S_8^1, $T_{S_8^1 \to S_8^2}(x)$, followed by the transformation of S_8^2 to S_5^2 using transformation $T_{S_8^1 \to S_8^2}(x)$ as starting point, giving a total transformation: $T_{S_8^2 \to S_5^2}(T_{S_8^1 \to S_8^2}(x))$. By applying this transformation to the voxel values $S_5^2(T_{S_8^2 \to S_5^2}(T_{S_8^1 \to S_8^2}(x)))$, translation between S_5^2 and S_8^1 is compensated for.

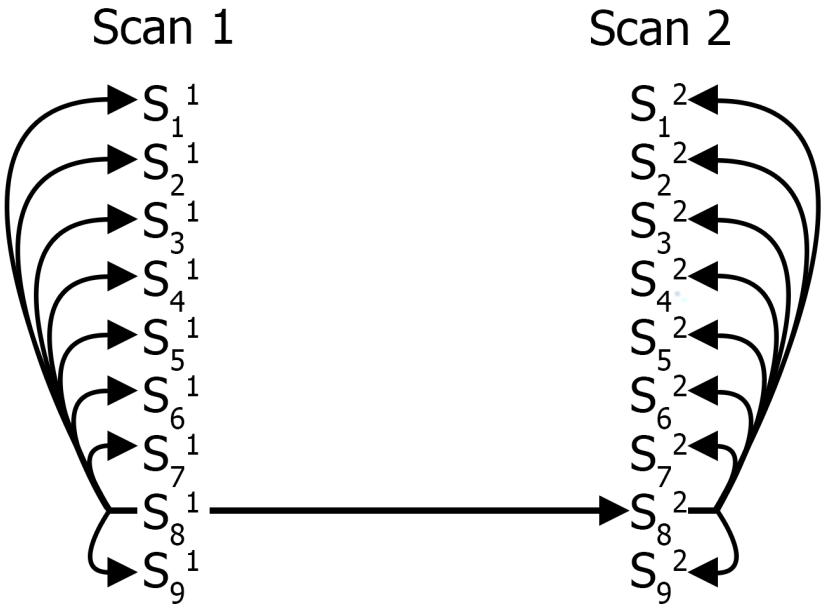

Figure 10: Pairwise registration in and between scan 1 and scan 2

2.3.2 Groupwise

Instead of registering one moving image to one fixed image, in groupwise registration all images from a single scan were transformed in the same optimization. The optimization of the transform parameters μ is given by:

$$\hat{\mu} = \arg\min_{\mu} \mathcal{D}(\mu) \tag{5}$$

where $\mathcal{D}(\mu)$ is the minimized dissimilarity metric, in which μ contains the transform parameters for all images g. For groupwise registration we used a metric proposed by Huizinga et al. [27]. This metric is based on Principal Component Analysis of the correlation matrix, which is insensitive to intensity scaling of the images.

$$\mathcal{D}_{PCA}(\mu) = \sum_{j=1}^{G} j\lambda_j(\mu) \tag{6}$$

λ_j, in Equation 6, is the jth eigenvalue of the correlation matrix which is summed over G. The dissimilarity metric promotes that as much variance as possible is explained by a few large eigenvalues.

All images from a given scan were registered to a mean space $\bar{S}_G^p$, where p is the scan number and G is a set of used images $\{1....G\}$. This mean space contains the groupwise registered images. As a result of this registration, intrascan alignment was achieved.

For interscan alignment, the same method as in pairwise interscan registration was used. In order to do so, the mean space images were transformed back to image 8. Doing so, the interscan transformation, $T_{S_8^1 \to S_8^2}(x))$, can be applied for interscan alignment. An additional advantage by using the same interscan transformation, is that it made comparison between the registration methods easier, since registration results in both methods are given in the image space of S_8^1.

As an example transformation, image 5 in scan 2 was firstly transformed to the mean space image A_2, giving transform parameters $T_{\bar{S}_G^2 \to S_5^2}(x)$, see Figure 11. Hereafter the inverse transformation of image 8 to the mean space image was used $T_{S_8^2 \to \bar{S}_G^2}(x)$. Followed by the interscan transformation, similar as in pairwise registration ($T_{S_8^1 \to S_8^2}(x)$). Giving a total transformation $S_5^2(T_{\bar{S}_G^2 \to S_5^2}(T_{S_8^2 \to \bar{S}_G^2}(T_{S_8^1 \to S_8^2}(x))))$, that aligned both inter- and intrascan.

2.3.3 Multi pairwise

The third method that we propose, is multi pairwise registration. Multi pairwise registration was performed interscan, and has as advantage that it utilizes all available images in the registration optimization, as opposed to using only one fixed and moving image to perform interscan registration, as was the case in the previously discussed methods. The images were transformed to mean spaces $\bar{S}_G^1$ and $\bar{S}_G^2$, as shown in Figure 12 using groupwise

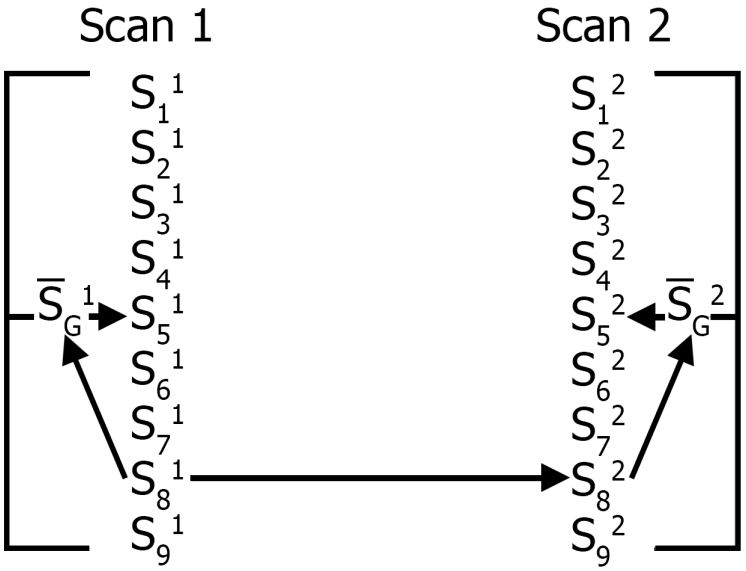

Figure 11: Groupwise registration in scan 1 and scan 2, and pairwise registration between scan 1 and scan 2

registration as was discussed in the previous subsection.

The optimization of the transform parameters in multi pairwise registration is given as:

$$\hat{\mu} = \arg\max_{\mu} \sum_{g=1}^{G} \lambda_g \mathcal{S}_g(\bar{S}_g^1(x), \bar{S}_g^2(T_g(x))) \tag{7}$$

given T_g a parametrization of μ. The similarity between two images with the same index g in scan one and two is summed over all images g. The contribution of the similarity between a given pair $\bar{S}_g{}^1(x), \bar{S}_g{}^2(T_g(x))$ in the optimization is weighted by λ_g. In our case the weight of each pair in the optimization was set equal. The metric used in the optimization is based on mutual information.

As an example, for image 5 in scan 2 the transformation can be written as $S_5^2(T_{\bar{S}_G^2 \to S_5^2}(T_{\bar{S}_G^1 \to \bar{S}_G^2}(T_{S_8{}^1 \to \bar{S}_G^1}(x))))$. $T_{\bar{S}_G^2 \to S_5^2}(x)$ describes the groupwise registration in scan 2, $T_{\bar{S}_G^1 \to \bar{S}_G^2}(x)$ the multi pairwise registration between mean spaces $\bar{S}_G^1$ and $\bar{S}_G^2$, and $T_{S_8{}^1 \to \bar{S}_G^1}(x)$ is the transformation to reference image S_8^1.

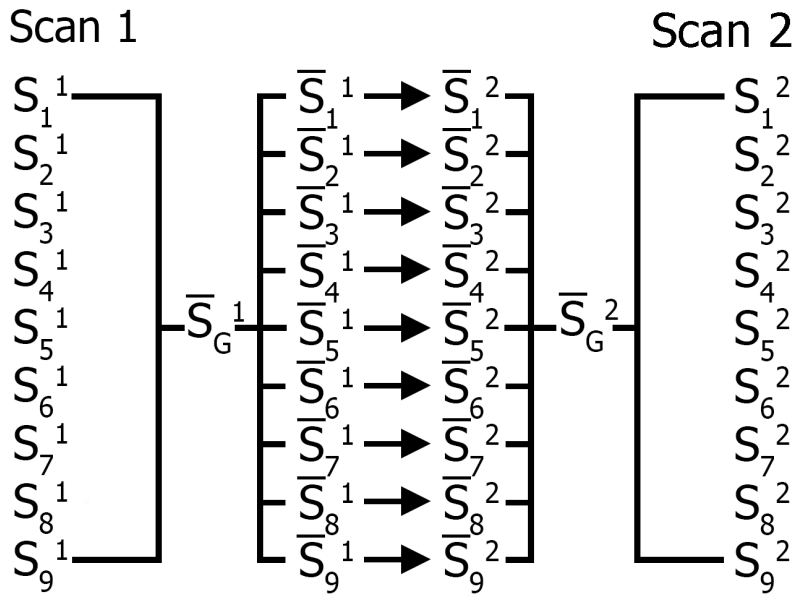

Figure 12: Groupwise registration in scan 1 and scan 2, and multi pairwise registration between scan 1 and scan 2. The multi pairwise registration gives one transformation for all image pairs

2.3.4 Registration settings

Elastix was used to perform the registration [35]. In each method described above, intrascan registration was performed using a non-rigid B-spline transformation. Interscan registration was performed in two stages. Firstly, a rigid Euler transform was applied, and secondly a non-rigid B-spline transformation was used. The B-spline gridsize was 15mm, which was optimized by van 't Klooster et al. [28]. The cost function is optimized using adaptive stochastic gradient descent, as proposed by Klein et al. [37].

All three methods were evaluated in the image space of $S_8{}^1$, as to make a fair comparison between the registration methods.

2.4 Mapping

Mapping of T_1 and T_2 was performed by fitting a mathematical model to the data of each voxel. This mathematical model contains the signal model

which determines the signal intensity for given settings. In the following subsections S contains the MR signal for a voxel x over all images G.

2.4.1 Signal model

The signal models in Equations 1, 2 and 3 can be rewritten into one function that describes the complex signal intensity as a function of the given parameters, for each of the used preparation modules. This function is given by:

$$S = Ae^{-T_E R_2}(1 - Be^{-T_I R_1} + (B-1)e^{-R_1(T_R - T_E)}) \tag{8}$$

where T_E, T_R, T_I for each image are given in Table 1.

Usually the magnitude signal is used to estimate the signal model parameters, as was discussed in the introduction. The magnitude signal of the complex signal given in Equation 8, is given by:

$$S = |Ae^{-T_E R_2}(1 - Be^{-T_I R_1} + (B-1)e^{-R_1(T_R - T_E)})| \tag{9}$$

For the inversion prepared images $T_E = 0$. When $T_E = 0$, the signal model in Equation 9 changes into:

$$S = |A(1 - Be^{-T_I R_1} + (B-1)e^{-R_1 T_R})| \tag{10}$$

Which is the same as Equation 3 in Section 2.1.4. For the spin echo prepared images, images 3 to 7 in Table 1, $T_I = 0$. Giving equation:

$$S = |Ae^{-T_E R_2}(1 - B + (B-1)e^{-R_1(T_R - T_E)})| \tag{11}$$

Since no inversion pulse is applied in this preparation, $B = 0$. This changes Equation 11 to:

$$S = |Ae^{-T_E R_2}(1 - e^{-R_1(T_R - T_E)})|, \tag{12}$$

which is the signal equation for spin echo prepared images, as described in Section 2.1.2. The last two image settings in Table 1 correspond to the saturation prepared images. For these images $T_I = 0$, giving Equation 11, and $B = 0$, giving signal model 12. T_E is zero as well for this preparation. Equation 12 can therefore be rewritten to Equation 13, which is the signal model for saturation prepared images as described in Section 2.1.3.

$$S = |A(1 - e^{-T_R\ R_1})| \tag{13}$$

The magnitude signal model may not suffice, when our acquisition scheme is used. We can explain this with the following example. For a given IR

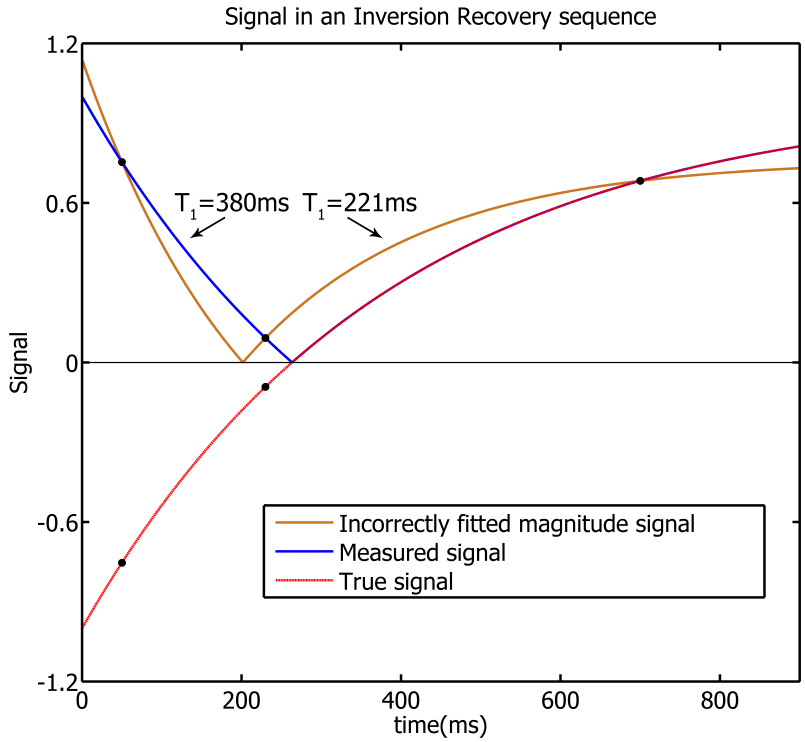

Figure 13: Measured and true longitudinal magnetization for an IR sequence

pulse sequence and tissue type, the real part of the complex signal may look like the red line in Figure 13. When the magnitude of this signal is used, we measure samples along the blue line. The black circles in this figure correspond to three measurement samples, taken at 50, 230 and 700 ms. Two curves may be fitted to this data, namely the blue and ochre curves. The measurement point around the null time, the time at which the signal is zero, is important for correct fitting. If our point at 230 ms is assumed to have negative magnetization, we would expect to fit the blue curve. If this point is assumed to have positive magnetization the ochre curve would be a possible fit. Based on whether a point has positive or negative magnetization at a certain time, the estimated T_1 can be incorrect.

Therefore, we propose to use a modified version of Equation 8, to allow the use of complex data. This change was made according to work of Barral et al. [19]. They proposed to change A:

$$A = r_a e^{i\phi_a} \tag{14}$$

In this case r_a, the scaled proton density is a real number, and ϕ_a is the transmit-receive phase. The complex signal model is then given by:

$$S = r_a e^{i\phi_a} e^{-T_E R_2}(1 - Be^{-T_I R_1} + (B-1)e^{-R_1(T_R - T_E)}) \tag{15}$$

2.4.2 Parameter estimation method

The signal model parameters were optimized using a maximum likelihood (ML) estimator. A ML estimator, maximizes the likelihood of a parameter x given the observed data y [38]:

$$\hat{x} = \arg\max_x \log(L(x|y)) \tag{16}$$

For our problem, using magnitude data, optimization of the signal model parameters θ can be written as:

$$\hat{\theta} = \arg\max_\theta \log(Rice(I|S(\theta))) \tag{17}$$

where the loglikelihood of the estimated magnitude signal $S(\theta)$ given the true magnitude signal I and a Rician distribution, was maximized. θ is a vector containing all signal model parameters that were estimated. When the complex signal model was used, the optimization is given as:

$$\hat{\theta} = \arg\max_\theta \log(\mathcal{N}(I|S(\theta))) \tag{18}$$

where I and $S(\theta)$ are normally distributed. The optimization method is based on a trust region method, which approaches global optimization by minimizing a quadratic approximation of the cost function at each iteration of the estimator. The estimated decrease in cost function, by assuming a quadratic shape of the optimization problem, is compared with the actual decrease in cost [39]. If the ratio between the predicted and actual decrease in cost function is in agreement, we can conclude that the quadratic approximation of the cost function is correct and we adopt the predicted step in parameter change. The trust region size is maintained or increased. If the agreement between predicted and actual decrease in cost function is poor, we can conclude that the current trust region can not be approximated by a quadratic model and the trust region is therefore shrunk [39]. Eventually the cost function reaches an optimum and no step can be taken that further decreases the cost.

The optimization also used a preconditioner. Preconditioning is an attempt to scale the quadratic form of the optimization to make it more spherical. A spherical optimization problem is faster to solve than a more ellipsoid

shaped optimization problem.

Before optimization of the signal model parameters, θ is initialized for each voxel using a search in a Halton sequence [40]. A Halton sequence generates points from a range of values in a quasi-random fashion, for a more even coverage over the set range, than would be the case when random samples are drawn. The range of values are user-defined, by giving a maximum and minimum value for each parameter. The parameter vector that results in the lowest cost, is used as initial value for the optimization.

In the following two subsections, we propose two methods that use the ML estimator and trust region method to estimate the signal model parameters. One in which B was kept constant and one in which B was estimated and spatially regularized.

2.4.3 Scenario 1: Constant B

In the first proposal, θ consists of four signal model parameters, namely: r_a, ϕ_a, R_1, R_2. B was set constant during optimization. The acquisition scheme was only optimized for T_1 and T_2 accuracy per unit of scan time, and not for accurate estimation for B. By setting B constant, the complexity of the parameter estimation decreases and we do not suffer from an ill-posed unknown B.

The estimation of the signal parameters from the registered images can be described by a pipeline. A visual representation of this pipeline is given in Figure 14. As described in the previous subsection, the signal parameters were initialized by performing a search in a Halton sequence. Hereafter, these parameters were optimized in a voxelwise manner. Two subsequent optimizations of the signal model parameters performed optimization in a blockwise manner. In blockwise optimization, multiple voxels are optimized with a single cost function. E.g. all the voxels present in the white block, given in Figure 15, are optimized with one cost function. After the voxels in the white block are optimized, the block is moved along one direction, giving the position of the red block. The voxels in this block are optimized, before the block is moved to the position of the blue block. This process continues until the block has moved across all spatial dimensions in the ROI. Blockwise optimization enables spatial coupling of the estimation of the signal model parameters. An optimum is found globally for the parameters of a block, as opposed to optimal parameters per voxel. A step in parameters is taken for all voxels in a block. There is no coupling in the optimization between

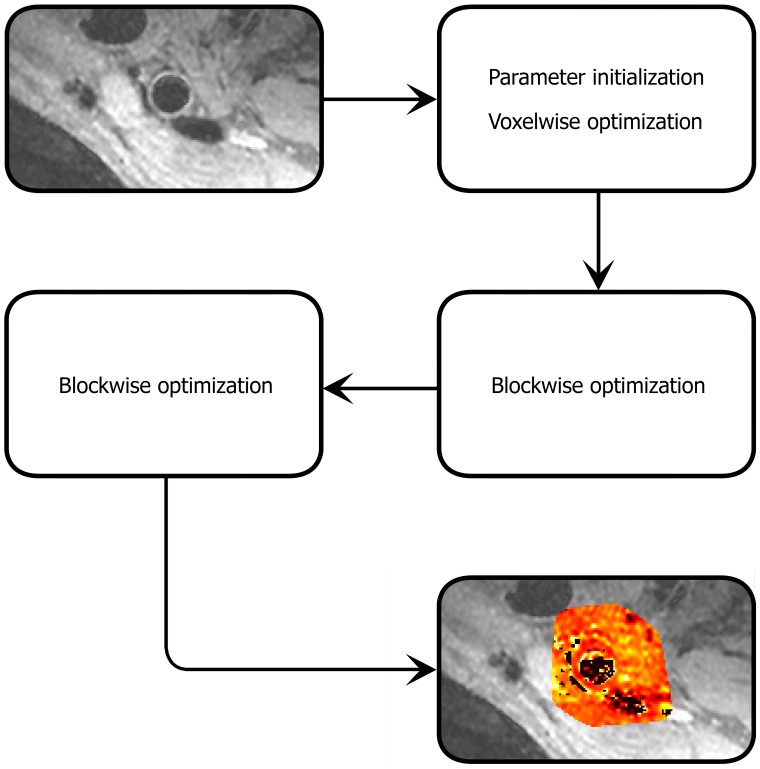

Figure 14: Flowchart representing the mapping processing pipeline for scenario 1

blocks. For instance, the optimization of the white block in Figure 15, does not take into account that the voxels in the red block also get optimized after the optimization of the white block. In order to couple the optimization of all blocks, multiple iterations of the blockwise fitting or overlap of blocks, were needed to achieve convergence of the optimization.

After two iterations of blockwise fitting, the final optimized parameters were used for evaluation of the carotid wall T_1 and T_2.

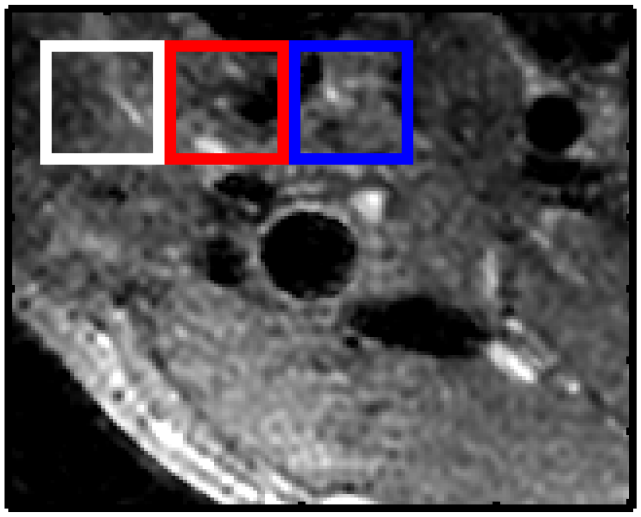

Figure 15: Three example blocks used in blockwise fitting

2.4.4 Scenario 2: B estimation and regularization

Setting B constant may induce a bias in the mapping results, and may give an incorrect representation of the true parameters (see Appendix C). Therefore, we propose to estimate B in this scenario. We also included the use of prior information of the signal model parameters in the estimation. Prior information can give insight on the spatial behaviour of a certain parameter, i.e. what values are expected in certain tissues, how many variability is expected in a certain ROI and what distribution is expected per parameter. We expect that ϕ_a, B and σ are slowly spatially varying, where σ is the noise level in the image. The CUBE readout sequence is based on spin echo, which refocuses phase accumulation due to variations in B_0, the main magnetic field [41]. Slow variation in ϕ_a can be caused by non centering of the echos in the readout window, which induces a phase gradient in the spatial dimensions. B is expected to be slowly varying, since adiabatic inversion pulses were used that are not influenced by inhomogeneities in the magnetic field [34]. From an early experiment, shown in Figure 22.B, where B is not spatially regularized, we observed that B was noisy and highly spatially varying. We therefore propose to spatially regularize both B and σ. ϕ_a showed (Section 4.2) to be slowly spatially moving, and thus did not require spatial regularization. When prior information is included and regularization is applied, we propose the following optimization for θ:

$$\hat{\theta} = \arg\max_{\theta}(\log(\mathcal{N}(I|S(\theta))) + \lambda\ \mathcal{L}(\theta) + \lambda_\sigma\ \mathcal{L}(\ln(\sigma);\theta) + \mathcal{P}(\theta)) \qquad (19)$$

a maximum a posteriori (MAP) estimator, where θ contains r_a, ϕ_a, R_1, R_2, B. The second argument in the equation contains the regularization term where the Laplacian $\mathcal{L}$ of the parameters is weighted by λ. The third arguments gives the regularization term of the Laplacian of $\ln(\sigma)$ optimized for θ, weighted by λ_σ. The fourth argument is the prior, containing information on the distribution of each parameter. In the following subsections the changes that were made in the cost function (Equation 19), as well as changes in the preconditioner are explained.

Spatial regularization and global estimation

Spatial regularization was achieved by adding a penalty term to the cost function, given by the second argument in Equation 19. Here, the Laplacian of the parameters is weighted by λ. A larger weight λ, increases the contribution of the Laplacian to the cost function, limiting the amount of spatial variation.

It is assumed that B and σ are slowly varying across the spatial dimensions, given the adiabatic pulse, discussed in Section 2.1.4. In order to correctly fit a global, slow varying B, we chose to use global estimation. In global estimation, a cost function is not optimized blockwise or voxelwise, but is optimized including all voxels in the ROI. With global estimation we expect to not suffer from spatial decoupling of the estimation of B due to blockwise fitting, but to fit a smooth B to the ROI.

Prior

The prior $\mathcal{P}$ is the last term in Equation 19. The prior specifies *a priori* information on the distribution of the parameters [18]. For simplicity, we assumed that the signal model parameters could be modeled by a normal distribution with a mean μ and standard deviation σ. Parameter estimates that are far away from the mean of this distribution, have a low probability, and high penalty in the prior.

In order to avoid bias due to the choice in distribution, we have chosen a standard deviation that covered more than the expected range of parameter values. By setting the prior, voxels with parameter values that are unlikely according to the prior, are penalized and pulled towards the mean of the distribution during optimization, even though the standard deviation of the prior distribution is larger than the expected range.

Preconditioner

As was discussed in Section 2.4.3, the preconditioner is based on the mean of the Hessian of the parameters, and attempts to scale the parameters to speed up the optimization. When global optimization is used, the mean of the Hessian is calculated over all voxels. The mean of the Hessian is heavily influenced by voxels where an incorrect fit with unrealistic parameter values is found. Voxels where R_1 and/or R_2 are strongly negative and r_a is close to zero can give a proper representation of the signal, but are by no means realistic. These voxels are located in the vessel lumen, where the signal intensity is low, and noise level is relatively high. In such outlier voxels the Hessian is disproportionate to the Hessian of voxels with realistic parameter values, which can have a large impact on the mean Hessian over all voxels.

When the mean of the Hessian is relatively high for one parameter, the allowed change in this parameter in the entire optimized volume is close to zero. In order to avert problems with the preconditioner due to the parameters of outlier voxels, we propose to compute the mean of the Hessian only on voxels that have realistic values, where R_1 is between $1/3$ and $10s^{-1}$ and R_2 is between 10 and $100s^{-1}$. By doing so, a single outlier voxel does not have influence on the optimization of the other voxels.

We also propose to smooth the preconditioned parameters using a filter. When regularization is applied during the optimization, the optimization can be sped up by smoothing the preconditioned parameters. Doing so, improves the condition number of the preconditioner. The condition number is a measure for the impact of a change in parameter values to a change in cost. Smoothing the preconditioned parameters improves the condition number and the optimization of the parameters. Smoothing is performed using a 1D filter to the preconditioned parameters, where the smoothed preconditioned parameter $y(n)$ at point n is given by:

$$y(n) = x(n) + \alpha x(n-1) \tag{20}$$

where $x(n)$ is the non smoothed preconditioned parameter at point n. α determines the strength of the smoothing. The spatial filter is based on an autoregressive model of order 1.

Signal model adaptation

The direction of the steps taken by the trust region method were based on the derivative of the signal to the signal model parameters, $\frac{\delta S}{\delta \theta}$, i.e. how much the signal changes by a change in parameter values. Over the entire range of realistic parameter values it is expected that a change in parameters changes the signal. With the current signal model, Equation 15, this is not completely possible. In Figure 16, $\frac{\delta S}{\delta r_a}$ is given for a range of R_1 for all nine images. The parameters are set at: $r_a = 100$, $\phi_a = 0$, $B = 1.85$, R_2=20. When parameter R_1 goes to zero, $\frac{\delta S}{\delta r_a}$ tends to zero as well. This means that when R_1 is close to zero, no efficient step can be taken for r_a that can change the signal, since r_a and S are decoupled.

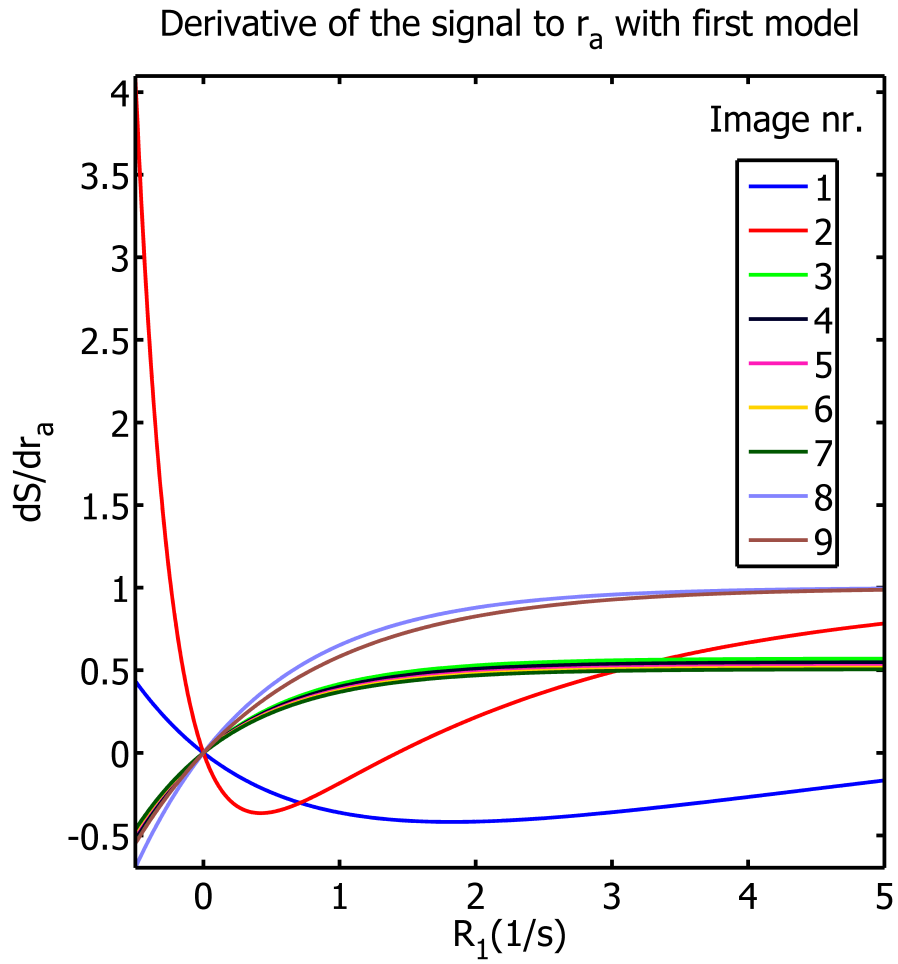

Figure 16: Derivative for r_a for a range of R_1 given the first signal model

In order to create a smooth and continuous derivative $\frac{\delta S}{\delta r_a}$ over a large range of R_1, an adaption in signal model is required. By dividing r_a by R_1, as given in Equation 21, continuity of the derivative is achieved. The derivative $\frac{\delta S}{\delta r_a}$ is non-zero around $R_1 = 0$, see Figure 17.

$$S = \frac{r_a e^{i\phi_a}}{R_1} e^{-T_E R_2}(1 - Be^{-T_I R_1} + (B-1)e^{-R_1(T_R - T_E)}) \tag{21}$$

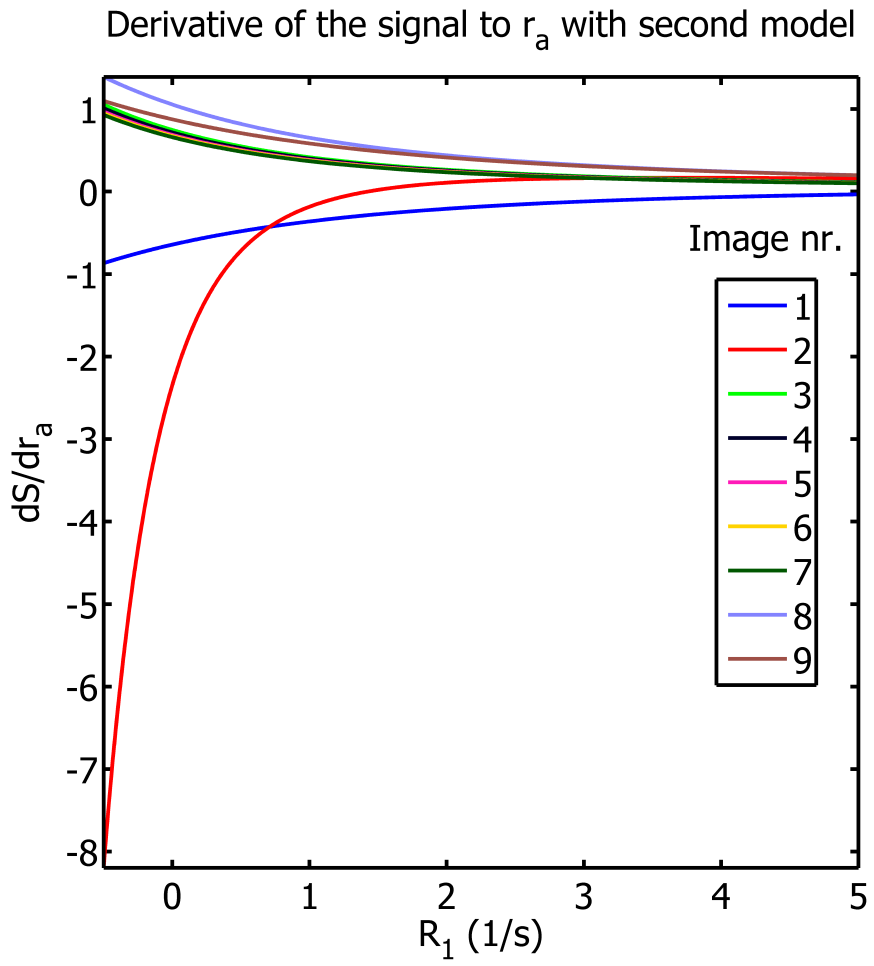

Figure 17: Derivative for r_a for a range of R_1 given the second signal model

Data substitution for unrealistic voxel values

Voxels with unrealistic parameter values can also have a negative impact on how steps are taken by the trust region method. As discussed in the previous subsection the trust region method optimizes the signal model parameters

based on $\frac{\delta S}{\delta \theta}$. When there are outlier voxels with large parameter values, e.g. R_1 and R_2 are 1000 times larger than the surrounding voxels, the trust region method can find a relatively large step in parameter values, due to a large gradient for these parameters. It assumes that the biggest change in cost function can be made by changing the parameter values of these voxels, voxels that are of no interest, since they are located in low SNR regions such as the vessel lumen. In order to avert the trust region method to only optimize these voxels we propose to replace the data and θ for these voxels imposing synthetic values that have minimal impact on the optimization of the neighbourhood. The data was created using parameter values given by the mean of the initial value range used in the Halton sequence. r_a was set to 0.1 times the median of r_a in the optimized volume, to lower the SNR of these voxels, and thus their contribution in the optimization.

Flowchart scenario 2

The estimation of the signal model parameters using scenario 2, can be visualized with the flowchart given in Figure 18. In this flowchart the first three optimization steps are similar as for scenario 1. In these steps parameters are initialized and optimized voxelwise and blockwise. During these steps, the adjustments proposed in this section are used. B is kept constant during the voxelwise estimation, as to avert spatial decoupling of the estimation of B during this step. In the next optimization step, B is optimized using the constant B from the voxelwise estimation as initialization.

In addition, four extra optimization steps are included that globally optimize the signal model parameters. It is expected that one global optimization should suffice, but to rule out termination of the optimization before an optimum is found, a total of four global optimization iterations are executed. As discussed in the previous subsections, global optimization is performed to estimate a smooth and continuous B for the ROI.

2.5 Cramer Rao Lower Bound

For the evaluation of the estimated parameters in the carotid wall, the Cramer Rao Lower Bound (CRLB) of the parameters was used. The CRLB gives the lower bound of the variance of an unbiased estimator [42]. In this thesis, the CRLB was used as a weight to evaluate the mean T_1 and T_2 in the carotid wall. The weighted mean is given by:

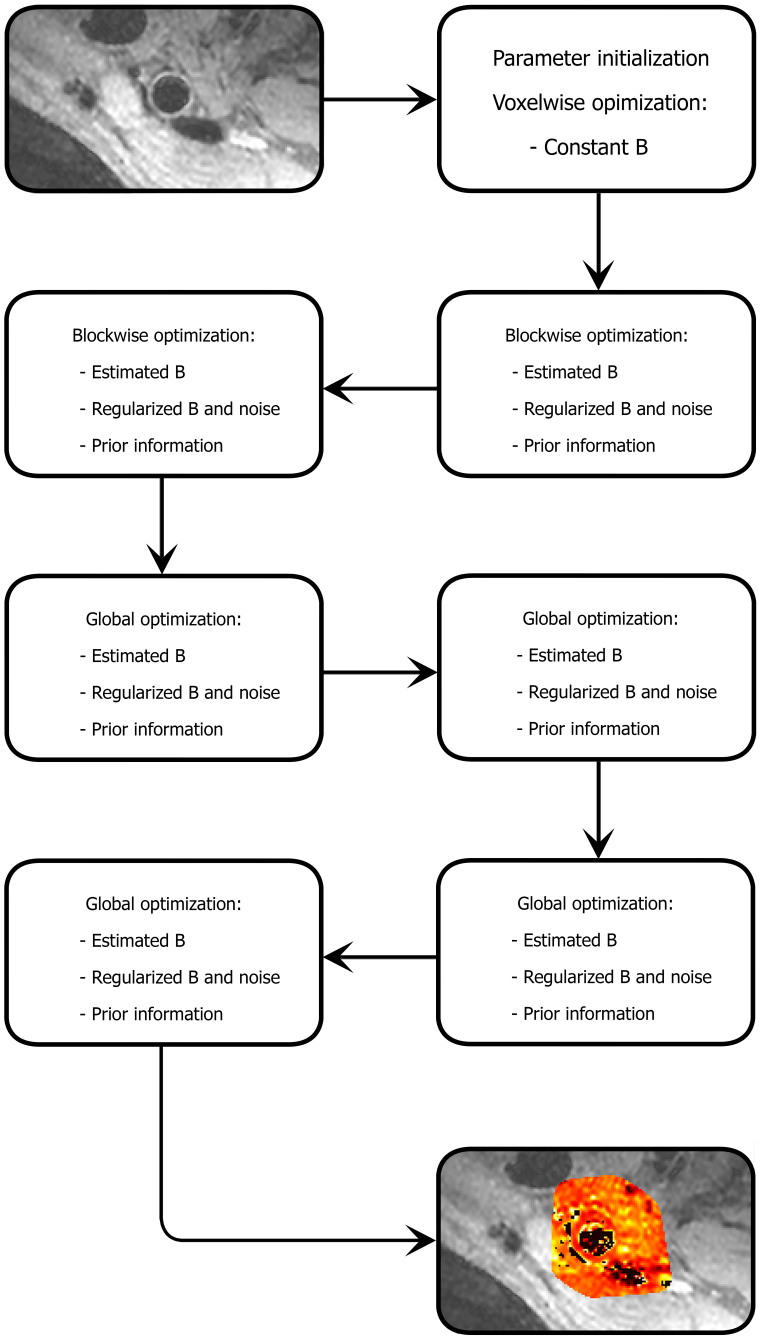

Figure 18: Flowchart representing the mapping processing pipeline for scenario 2

$$\bar{T}_k = \frac{\sum_x^N T_k(x) w(x)}{\sum_x^N w(x)} \tag{22}$$

where T_k is T_1 or T_2, and $w(x) = 1/\text{CRLB}(x; T_k)$ the CRLB at point x for parameter T_k.

3

Experimental setup

In the following subsections the experiments are described that are required to evaluate the reproducibility. As was discussed in the introduction, the feasibility of the complex signal model will be firstly tested on simulated data (Section 3.1) and secondly on hardware phantom data (Section 3.2). In Section 3.3, the experimental setup for the volunteer studies is given, with which we want to evaluate three different registration methods, and the influence of B on the reproducibility of T_1 and T_2.

In this thesis, a GE Discovery MR750 3.0T MR scanner was used for the acquisition of MR images. The size of the FOV was 16 cm in the frequency direction, and 14 cm in the phase direction. The image size in the frequency direction was 512 voxels and 448 voxels in the phase direction, where the voxel size in these directions was 0.3mm. A total of 16 slices were acquired, with a slab thickness of 2mm. Parallel imaging was used to acquire these images, where an ARC factor of 2 was used [43].

3.1 Complex signal model testing: Monte Carlo experiment

In this experiment the aim was to evaluate the performance of both the complex and magnitude signal model using simulated data. Data was generated using the complex signal model (Equation 15) and the optimized acquisition settings, for a range of T_1 values (100 through 1500ms). B was set to 1.9, the

unprepared magnitude, r_a, at 1000 and $\phi_a = 0$. Zero mean Gaussian noise with σ=33, was added to both the real and imaginary parts for each of 10.000 independent realizations.

The data was fitted by both the complex and magnitude signal model. For the magnitude model, the magnitude of the complex data was used. The distribution of the estimates for each given T_1 was inspected visually on bimodality. A threshold that separates the data of both distribution modes was manually set. The mean and standard deviation of both modes was evaluated.

3.2 Complex signal model testing: Hardware phantom

The performance of the complex signal model (Equation 15) and the magnitude signal model (Equation 9) was also evaluated using a hardware phantom consisting of twelve tubes. Each tube contained an unknown amount of agarose, for T_2 shortening, and $GdCL_3$ for T_1 shortening. It is assumed that the contents in the tubes are uniformly distributed.

The pulse sequence settings as described in Section 3.3 were also used for the acquisition of images of the hardware phantom. For the hardware phantom no image registration was required, since the phantom remained still during the acquisition of all images.

For the fitting of the acquired data, scenario 1 was used, with $B = 1.95$. A blocksize of 3x3x3 and an overlap of one was used for the blockwise optimization.

For evaluation of the results, the mean T_1 and T_2 for each tube, as well as the standard deviation, are given. We also visually evaluated the phase estimates to determine the presence of phase errors and/or effects of phase errors.

3.3 Volunteers

In this experiment nine volunteers were scanned using the settings described in Section 2.1.5. Each volunteer was scanned twice to be able to evaluate reproducibility of T_1 and T_2 maps. Between each scan, the volunteer was

taken off the table for a short period of time. The influence of registration and mapping methods was evaluated on the T_1 and T_2 of the carotid wall.

For evaluation of the estimated signal model parameters, a mask was manually drawn on the carotid wall in one scan. This mask was used to evaluate the results for both scan and rescan. We have given the weighted mean for T_1 and T_2, calculated using Equation 22.

3.3.1 Evaluation of registration methods

In this experiment the goal was to evaluate the performance of each registration method described in Section 2.3.

For parameter estimation, the optimization scheme given in scenario 1 (Section 2.4.3) was used, with $B = 1.95$, so only five parameters (r_a,R_1,R_2, ϕ_a and σ) are estimated.

The performance of the registration methods was tested by evaluating T_1 and T_2 weighted mean between scan and rescan in the carotid wall.

3.3.2 B estimation and regularization

In order to test the dependence of the T_1 and T_2 maps on the value of B, we performed an experiment using scenario 2, where B was estimated and spatially regularized using the MAP estimator (Section 2.4.4). Image registration was performed using the multi pairwise approach.

In this experiment, B was set constant at 1.85 during the voxelwise optimization. In the following six iterations, B was estimated and regularized. In blockwise optimization, a blocksize of 3x3x3 voxels with an overlap of one was used.

For the regularization, four weights for B were used, namely 0, 50, 1000 and 10.000. The weight for the Laplacian of σ was set to 50. α, the autoregressive filter variable, was set at 0.5.

For the evaluation of the results, the T_1 and T_2 weighted mean was calculated using the carotid wall mask. The regularization weights for B were evaluated by visual inspection of the B maps.

3.3.3 Patient example

As an example, we also scanned a patient that had carotid plaque. The patient was scanned only once, but with the same pulse sequence settings as described in Section 2.1.5. For registration we used the multi pairwise approach. Mapping was performed using the method described in Section 2.4.4.

4

Results

4.1 Complex signal model testing: Monte Carlo experiment

Figure 19 shows the mean and standard deviation for observed modes of T_1 estimates, given both signal models. From this figure we can clearly see that over almost the entire range of T_1, bimodality occurs when the magnitude model is used for fitting the data. For a true T_1 of 300ms, bimodality is not observed. When the complex model is used, the mean of the estimates corresponds to the true T_1. For both models, the spread in T_1 estimates increases as the true T_1 increases.

4.2 Complex signal model testing: Hardware Phantom

In Figure 20, the resulting T_1 map is given for a cross section of the hardware phantom tubes. In the top row, the magnitude model is used, and in the bottom row the complex signal model is used. As we can see in Figure 20.A, the T_1 maps are not uniform in each tube. We would however expect the maps to be uniform for each tube, since the contents of the tubes are assumed to be homogeneous. For several T_1 there is ambiguity in the estimated results. In Figure 20.B one tube is magnified and we can clearly see two distinct T_1 modes. The mean and standard deviation of these two modes are 846.6±10.9ms and 541.5±8.7ms. When the complex signal model is used,

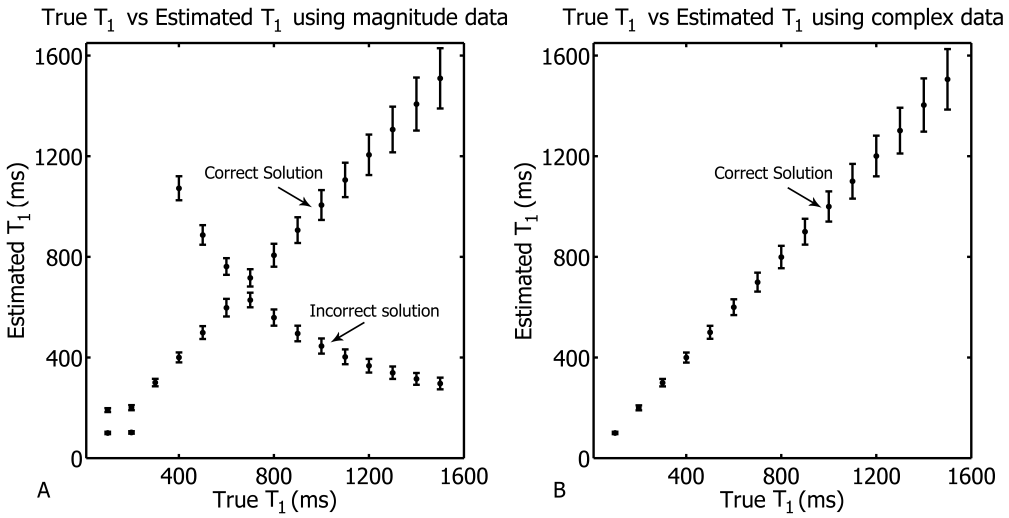

Figure 19: T_1 mean and standard deviation for using the magnitude and complex signal model, for fitting the simulated data

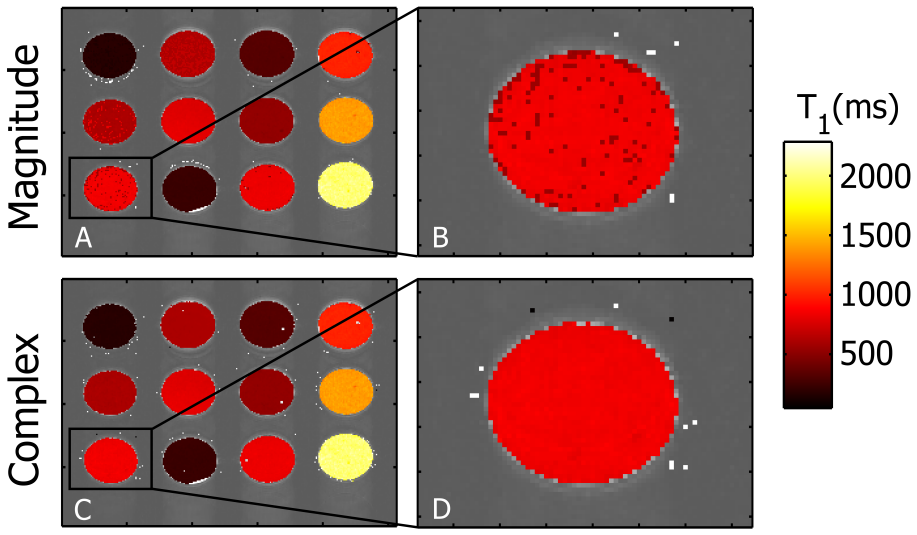

Figure 20: T_1 maps for a cross section of the hardware phantom, using the magnitude and complex model

Figure 20.D we no longer suffer from ambiguous results, and only a single mode is observed with mean 846.1±12.3ms.

The phase map, when using the complex signal model, is smooth and

slowly spatially varying, as can be seen in Figure 21. In the z-direction the phase ranges from -1 to 1 radians. In x and y there is also a gradient visible, roughly varying 0.5 radians over the range visible in this figure. There are no artifacts visible in this figure that could be caused by phase errors.

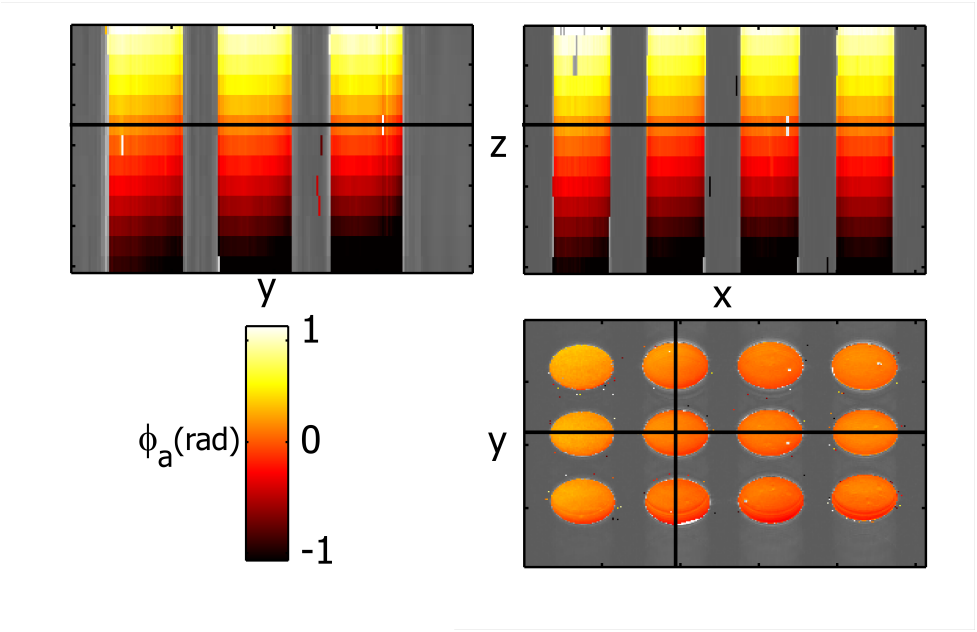

Figure 21: Phase map of the hardware phantom in all spatial dimensions

4.3 Volunteers

4.3.1 Evaluation of registration methods

In Tables 2 and 3, the estimated carotid T_1 and T_2 are given, using the previously described registration methods. For each of the nine volunteers, a weighted mean for T_1 and T_2 is given. The square root of the CRLB (sCRLB) of the weighted mean is also given in these tables.

Differences in T_1 between scan and rescan vary from 7 to 90ms, with as extrema a difference of 230ms for volunteer 38. The mean difference in T_1 between scan and rescan is 58.3ms, given a mean T_1 of 960.7ms. The differences between scan and rescan for T_2 do not follow the same pattern as in T_1, i.e. a larger T_1 weighted mean does not give a larger/lower T_2 weighted mean. For volunteer 38 the difference between scan and rescan in T_2 is the largest, 15ms, whereas the mean difference between scan and rescan over all

volunteers in T_2 is 6.3ms.

The T_1 values seem to be slightly closer between scan and rescan for the groupwise approach than when the pairwise approach is used, given the difference in weighted mean for volunteers 30, 31, 32, 35, 36 and 40. For the other volunteers an increase in difference between scan and rescan is observed. The difference between scan and rescan T_1 weighted mean is not significantly different between the pairwise and groupwise approach, t(8)=0.38,p=0.7115. The mean sCRLB remains the same between pairwise and groupwise. The mean of the difference in scan and rescan for T_2 remains the same when using both methods and the difference between scan and rescan T_2 weighted mean is not significantly different between the pairwise and groupwise approach, t(8)=0.13,p=0.904.

When the multi pairwise approach was employed, we can see that for volunteer 29, 30, 31, 32, 36, 38, the T_1 weighted mean is closer to that of scan 1 than when the groupwise method is employed. The mean of the differences between scan and rescan between pairwise and multi pairwise registration decreases from 58.3ms to 50.6ms. However, the difference between scan and rescan T_1 weighted mean is not significantly different between the pairwise and multi pairwise approach, t(8)=0.91,p=0.388. The T_2 weighted mean changes similar to the T_1 weighted mean between the registration methods. Only for volunteer 36, where the T_1 was closer for scan and rescan in multi pairwise than in pairwise registration, the T_2 is slightly further apart. For volunteer 41, the T_2 is closer together in multi pairwise than in pairwise registration, as opposed to a larger T_1 difference when multi pairwise registration is employed. The difference between scan and rescan T_1 weighted mean is not significantly different between the pairwise and multi pairwise approach, t(8)=0.22,p=0.835.

4.3.2 B estimation and regularization

B was regularized using four regularization strengths. In Figure 22B-E, the estimated B maps for a given ROI, using a regularization weight of 0, 50, 1000 and 10.000, is shown. In Figure 22.B, the B map is given for weight 0. In this case there is no spatial coupling of B, and estimated values for B range from 0.86 to 56.4, where values above $B = 2$ are physically impossible. In the carotid lumen, the substituted voxels can be clearly seen, where $B = 1.85$. In Figure 22.C, multiple modes are visible across the ROI, where B ranges from 1.49 to 2.00. When the weight is increased, around four to five modes remain,

Vol.	T_1 (ms)						
	Scan	Pairwise		Groupwise		Multi pairwise	
		Weighted mean	sCRLB	Weighted mean	sCRLB	Weighted mean	sCRLB
29	1	939.6	3.9	933.9	3.9	933.9	3.9
	2	962.4	3.7	969.6	3.7	963.8	3.6
30	1	858.3	4.8	923.2	4.9	923.2	4.9
	2	943.5	5.5	865.5	6.0	968.9	5.8
31	1	1012.3	6.5	1035.2	6.0	1035.2	6.0
	2	1028.2	5.7	1050.7	5.3	1036.8	5.3
32	1	897.0	5.6	903.7	5.6	903.7	5.6
	2	870.0	5.6	926.5	5.7	911.4	5.6
35	1	1021.0	3.8	1018.2	3.7	1018.2	3.7
	2	995.7	3.5	1001.6	3.4	999.3	3.5
36	1	969.1	5.2	979.1	5.2	979.1	5.2
	2	945.4	5.0	961.4	5.0	980.8	5.2
38	1	894.6	5.6	889.6	5.4	889.6	5.4
	2	1124.8	7.6	1133.3	7.3	1116.6	7.0
40	1	935.0	4.9	939.4	5.0	939.4	5.0
	2	1022.3	4.5	1002.1	4.5	1006.2	4.5
41	1	933.6	4.7	998.8	5.2	998.8	5.2
	2	940.6	3.4	966.8	3.4	942.5	3.4
mean		960.7	5.0	972.1	5.0	974.9	4.9
mean of dif.		58.3	0.7	56.0	0.8	50.6	0.7

Table 2: Weighted mean and sCRLB for T_1, for pairwise, groupwise and multi pairwise registration

and the range in B is significantly smaller (1.61 to 1.86). Increasing the weight to 10.000 gives a very smooth and continuous B map, with values between 1.65 and 1.85. Given the background in Figure 22.A, global estimation of B is not heavily influenced by the substituted voxels where B was set at 1.85, as was discussed in Section 2.4.4.

Table 4 shows the weighted mean for T_1 and T_2 when B is estimated and regularized, using a regularization weight of 10.000. For most volunteers the difference in T_1 between scan and rescan has increased, as well as a systematically higher T_1 weighted mean for each volunteer. This increase can more clearly be seen in Figure 23, where the weighted mean is given for T_1 and T_2, using scenario 1 and 2. Two points connected with a colored line represent the weighted means for scan and rescan for one volunteer. The red lines at each point represent the sCRLB for T_1 and T_2. The results for scenario 2 are

Vol.	T_2 (ms)						
	Scan	Pairwise		Groupwise		Multi pairwise	
		Weighted mean	sCRLB	Weighted mean	sCRLB	Weighted mean	sCRLB
29	1	39.2	0.2	39.3	0.2	39.3	0.2
	2	40.7	0.2	39.4	0.2	39.3	0.2
30	1	38.8	0.3	39.8	0.3	39.8	0.3
	2	38.4	0.3	37.1	0.4	40.0	0.3
31	1	41.3	0.4	40.3	0.3	40.3	0.3
	2	51.4	0.4	49.0	0.4	50.6	0.4
32	1	44.0	0.4	45.1	0.4	45.1	0.4
	2	36.5	0.3	37.3	0.3	37.5	0.3
35	1	37.9	0.2	37.0	0.2	37.0	0.2
	2	41.7	0.2	41.4	0.2	42.0	0.2
36	1	36.5	0.2	35.8	0.2	35.8	0.2
	2	42.3	0.3	40.8	0.3	42.2	0.3
38	1	34.2	0.3	34.6	0.3	34.6	0.3
	2	49.6	0.6	51.1	0.5	50.1	0.5
40	1	39.8	0.3	39.8	0.3	39.8	0.3
	2	44.5	0.3	42.9	0.3	43.7	0.3
41	1	44.8	0.3	44.2	0.4	44.2	0.4
	2	37.2	0.2	36.2	0.2	36.8	0.2
mean		41.0	0.3	40.6	0.3	41.0	0.3
mean of dif.		6.3	0.1	6.3	0.1	6.3	0.1

Table 3: Weighted mean and sCRLB for T_2, for pairwise, groupwise and multi pairwise registration

given in dashed lines and the results from the previous experiment, using scenario 1, are given in solid lines. This Figure clearly shows an increase in weighted mean for T_1, whereas the weighted mean for T_2 remains the same. For volunteers 30 and 41, the difference in T_1 weighted mean has increased to more than 200ms, where it was only a few milliseconds when B was kept constant. For volunteers 38 and 40 the difference in T_1 decreased up to 70ms. The weighted mean of T_2 is very much the same as when B was kept constant.

In Figure 24, the difference in parameters is given between two subsequent optimizations. Between the third and fourth optimization, the largest change in parameters is observed. The fourth iteration, is the first iteration that employs global optimization. Convergence is reached after seven iterations. T_1 changes only up to a few milliseconds between the last two iterations.

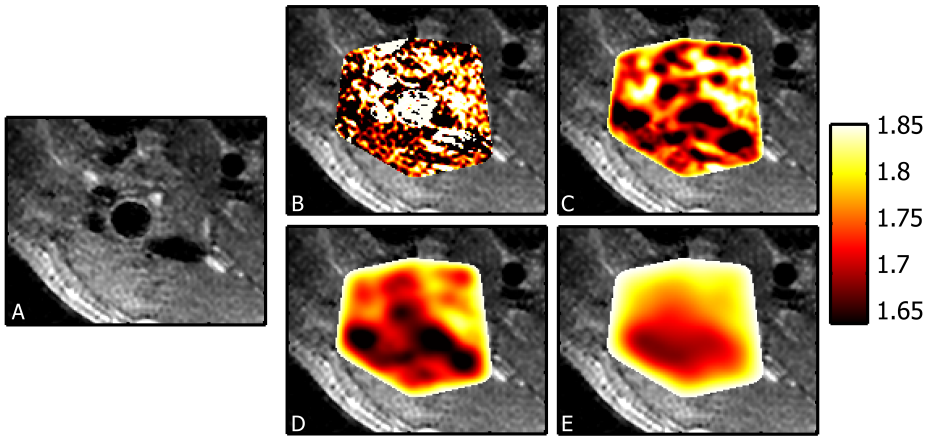

Figure 22: Inversion efficiency maps for various regularization weights. A: MR image, B: weight 0, C: weight 50, D: weight 1000, E: weight 10.000

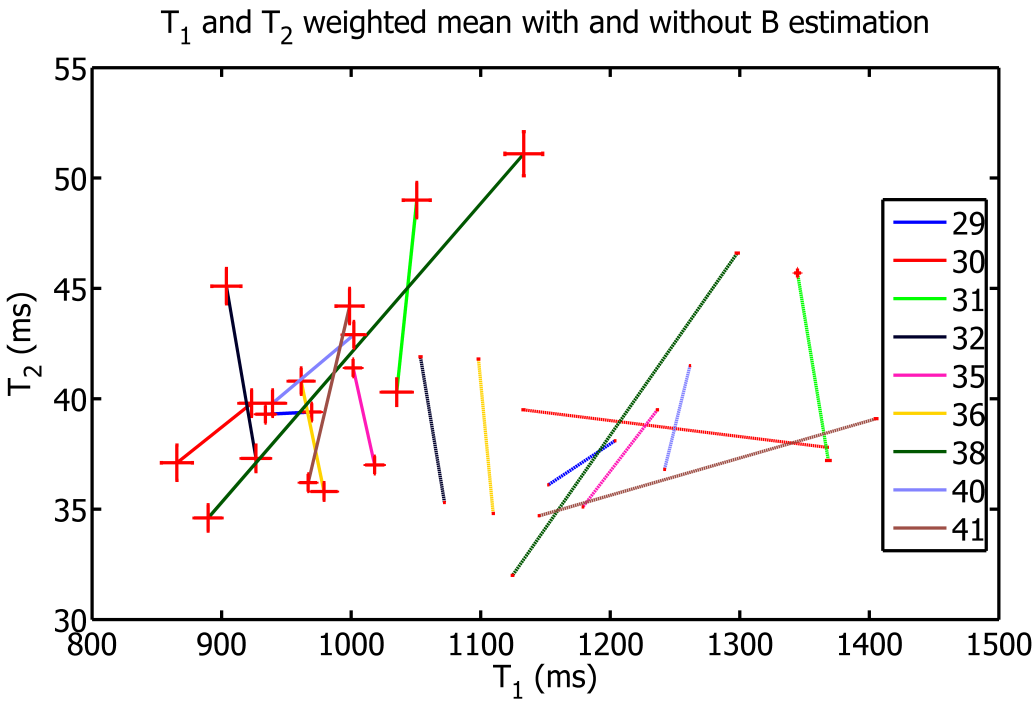

Figure 23: T_1 and T_2 weighted mean for scan and rescan for all volunteers. Scenario 1 multi pairwise where B is fixed: results given in solid lines, scenario 2 multi pairwise results where B was estimated and regularized: results given in dashed lines

Vol.	Scan	T_1 (ms)		T_2 (ms)	
		Weighted mean	sCRLB	Weighted mean	sCRLB
29	1	1152.2	0.4	36.1	0.02
	2	1203.8	0.5	38.1	0.02
30	1	1133.0	0.8	39.5	0.03
	2	1367.6	0.6	37.8	0.01
31	1	1368.4	1.3	37.2	0.03
	2	1344.6	1.3	45.7	0.08
32	1	1053.5	0.8	41.9	0.03
	2	1072.0	0.5	35.3	0.02
35	1	1178.9	0.5	35.1	0.03
	2	1236.4	0.6	39.5	0.03
36	1	1109.7	0.6	34.8	0.03
	2	1098.3	0.7	41.8	0.04
38	1	1124.6	0.7	32.0	0.02
	2	1298.0	1.0	46.6	0.04
40	1	1242.0	0.5	36.8	0.02
	2	1261.6	0.4	41.5	0.03
41	1	1405.2	0.9	39.1	0.03
	2	1145.0	0.5	34.7	0.02
mean		1210.8	0.7	38.5	0.03
mean of dif.		94.5	0.2	6.0	0.01

Table 4: Statistics for scan and rescan, and T_1 and T_2

As an example, the resulting maps for Volunteer 35 are given in Figure 25. The carotid wall can be clearly seen in the T_1 and r_a maps. The lumen of the vessel and substituted voxels have no clear effect on the global estimation of B, which is smooth and continuous throughout the ROI.

4.3.3 Patient example

The parameter maps for the patient are given in Figure 26. In the r_a map, an outline of the vessel lumen and outer vessel wall are given in green and blue respectively. The outline of the plaque is given in purple. The corresponding T_1 and T_2 maps show a clear decrease in T_1 and increase in T_2 in the observed plaque compartment.

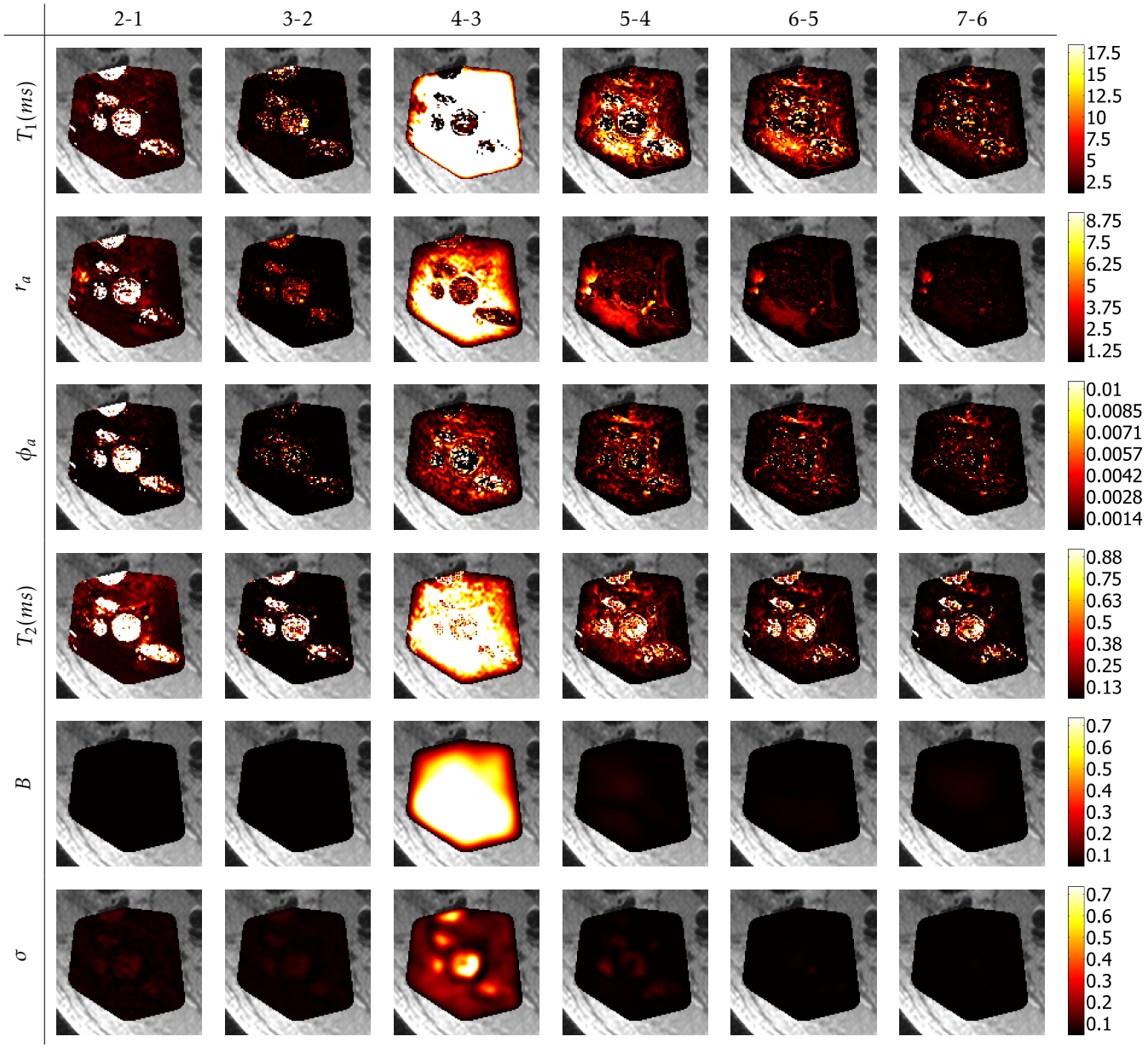

Figure 24: Absolute difference in parameters (row) between two subsequent iterations of the ML estimator (column)

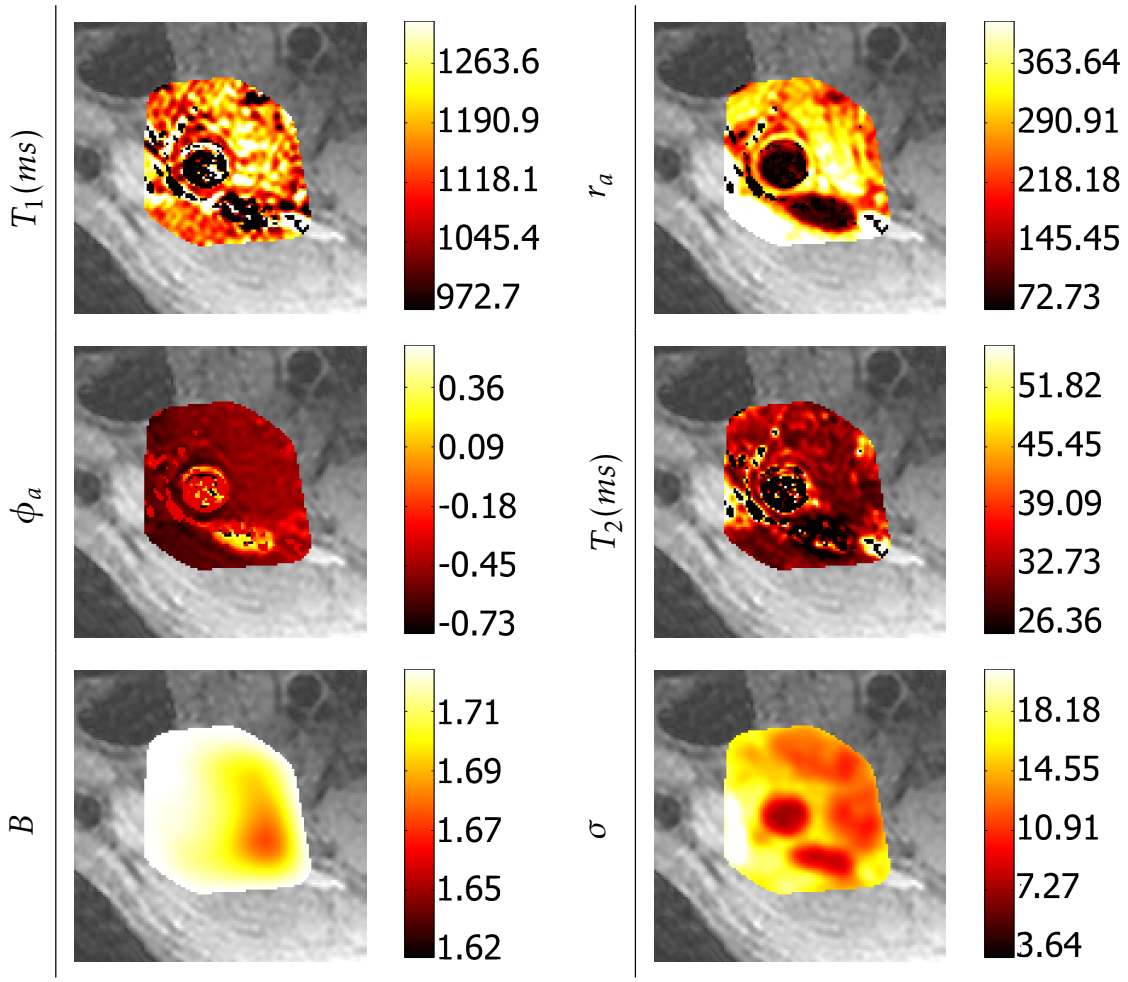

Figure 25: Parameter maps for a cross section of Volunteer 35

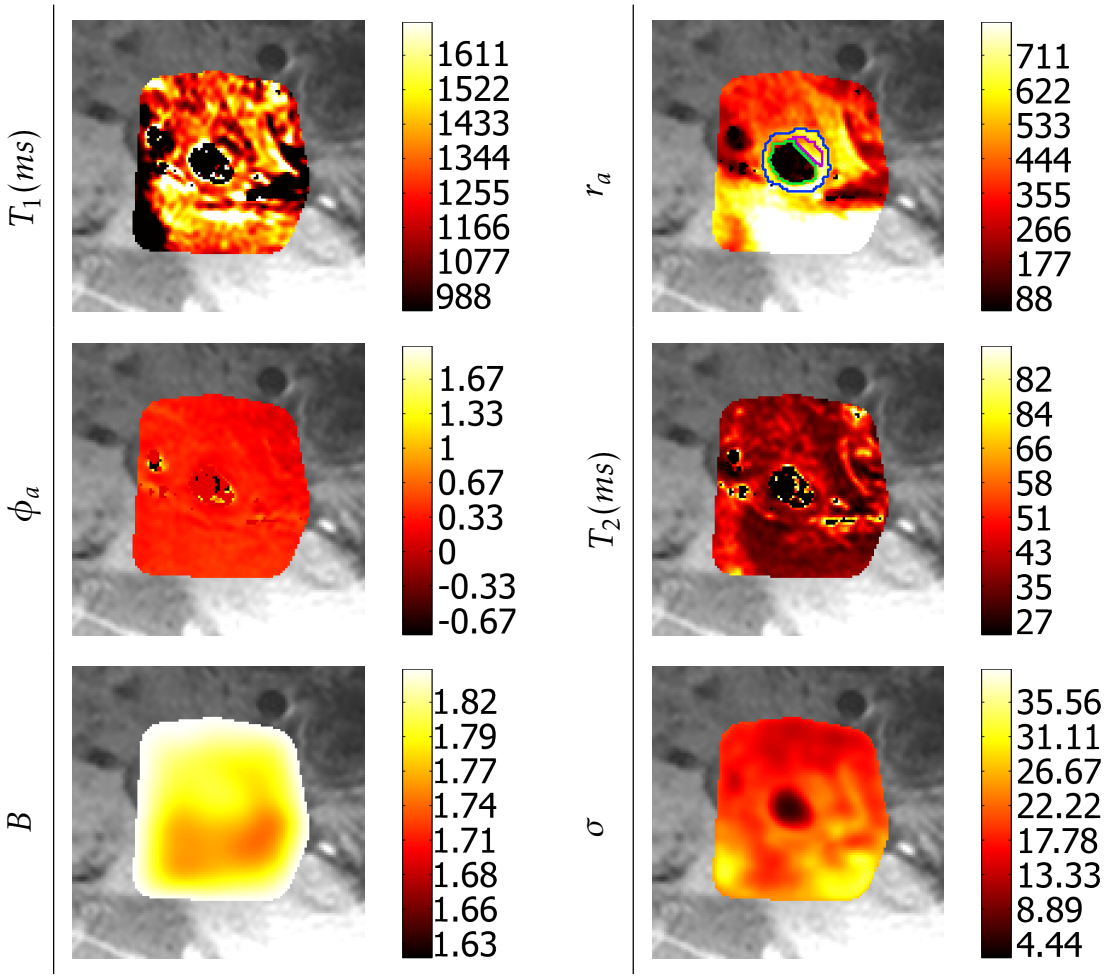

Figure 26: Parameter maps for a cross section of the patient

5

Discussion

Our findings demonstrate that the use of a complex signal model represents the acquired MR data better than the use of a signal model based on the magnitude signal. From the results in Section 4.1 and 4.2 we observed for various T_1, which correspond to possible T_1 present in carotid plaque, that ambiguity in estimated T_1 occurs when the magnitude signal model is used. Two solution modes are observed, see Figure 19, although only one mode is expected, that corresponds to the true T_1. Therefore reproducibility of T_1 estimation might be hampered when the magnitude signal is used. In plaque characterization using T_1 and T_2, it is not desirable to estimate ambiguous T_1 values in a homogeneous area. In this case, several voxels with incorrect T_1 might be classified as a different tissue. The use of complex data resolves the ambiguity in T_1 estimation and the inclusion of phase data in the estimation of T_1 and T_2 does not result in phase errors in the mapping results. The estimated ϕ_a is smooth and continuous over the spatial dimensions.

The difference in weighted mean for T_1 between scan and rescan, when evaluating the registration methods, shows an improvement in scan-rescan reproducibility when the multi pairwise approach is employed versus the pairwise approach (50.6ms vs. 58.3ms). This difference is not significant. However, the use of multi pairwise registration is recommended. The most important contribution of multi pairwise registration is that it uses all images in interscan registration, rather than relying on a single user defined image pair for interscan registration. The bias that might be introduced by choosing an image pair for interscan registration might jeopardize the validity of tissue

quantification.

Image registration on its own is an important preprocessing step in tissue quantification. If a voxel does not represent the same anatomical structure in each image, quantification of tissue parameters will be inaccurate. Future work can involve improvement of the registration. Exploring the use of other metrics and gridsizes might improve reproducibility of T_1 and T_2. We do have to take into account that in this study healthy volunteers were scanned. It is likely that patients suffer from more conditions and are therefore less likely to stay still in the scanner. In patient scans, other than shown in the example in Section 4.3.3, more motion artifacts were visible in the taken images than in volunteers. An increased amount of motion artifacts could make image registration harder and could hamper the quantitative assessment of plaque components. It is not known how large this influence can be.

The estimation of B has an impact on the estimation of T_1. The results in Section 4.3.2 show an increase in T_1 weighted mean when B is estimated and regularized. It is clear that there is a coupling between B and T_1. B was estimated between 1.65 and 1.85 when using a regularization weight of 10.000, resulting in a higher T_1 than when B was set constant at 1.95. The difference in estimated T_1 weighted mean is more than 200ms between scenario 1 and 2, even though B only changes up to 0.3. The implication of this is that a relatively small change in B results in a relatively large change in T_1. If B is not correctly estimated a difference in T_1 between scan and rescan can be expected. Since the acquisition scheme is not optimized for accurate B estimation, the incorrect estimation of B can potentially hamper the accurate quantification of T_1. Between scenario 1 and scenario 2, the sCRLB drops about a factor ten for both parameters. The lowest achievable variance for an unbiased estimator is smaller when scenario 2 is used, as opposed to when scenario 1 is used. Future work may show where this difference in sCRLB between both scenarios comes from, and why the sCRLB is so low for the parameters estimated in scenario 2.

The spatial regularization of B should aid in a global estimation of this parameter, but can be incorrect at the borders of the mask. As can be seen in Figure 22, the edge of the mask has a value of 1.85, the initial value of this parameter. When the carotid is close to the border of the mask, B is potentially incorrect in the carotid wall, which could impact the reproducibility of T_1. However, as the mask is drawn manually around the carotid, this is not

expected to be a serious limitation. There is a big advantage in using scenario 2 over scenario 1. Due to the estimation of B, a potential bias in results is averted. From our results, it becomes clear that a constant B for the entire ROI is an incorrect assumption.

The reproducibility of T_1 and T_2 suffices when the T_1 and T_2 difference between plaque tissues is larger than the observed inter volunteer difference. The difference in T_1 and T_2 between scan and rescan should not be attributable to difference in patient loading or coil positioning, but on difference in tissue type. Harteveld et al. [44] have determined the T_1 and T_2 of various plaque components, ex-vivo on intracranial arterial plaque using a 7T MR scanner. For lipids they estimated a T_1 of 838±167ms, for calcium a T_1 of 314±19ms, for fibrous tissue a T_1 of 583±161ms, for the fibrous cap a T_1 of 481±98ms and for the intracranial arterial vessel wall a T_1 of 436±122ms. We estimated the inter volunteer difference in T_1 at 94.5ms. Lipids and calcifications can most likely be correctly characterized with the current reproducibility.

Biasiolli et al. [13] estimated T_2 for multiple tissues, in-vivo using a 3T MR scanner. Yielding a T_2 of 56±9ms for fibrous tissue, 54±13ms for the tunica intima and media, 37±5ms for the LRNC, and 107±25ms for calcifications. With the current reproducibility, differences between calcifications and other tissues can be clearly seen. The difference between the LRNC and other tissues can possibly also be observed. The estimated interscan difference in T_2 is estimated at 6ms, which is roughly three times smaller than the difference between the T_2 of the LRNC and the T_2 of fibrous tissue and the tunica intima and media.

There is room for improvement in the reproducibility of T_1 and T_2. An estimation of B in the sternocleidomastoid muscle could potentially aid in scan-rescan reproducibility. The homogeneity and size of this muscle makes parameter estimation less dependent on registration results and influence of other tissues. A difference in B in this muscle between scan and rescan can help as an indicator for a potential difference in B in the carotid artery. Correcting for this occurring difference could improve the reproducibility in T_1 between scan and rescan.

The strong coupling between B and T_1 could potentially be resolved by changing the parametrization of the signal model, e.g. replacing B by a

parameter that is also dependent on T_1. Another solution could include a revision of the optimization of the acquisition scheme. Also optimizing for accurate B estimation could aid in better T_1 reproducibility. This would probably result in an increase in acquired images, and would have as disadvantage that total scan time increases. It is unfavorable to increase the total scan time, due to the chance of an increased number of motion artifacts in the last images caused by restless patients.

Even though a strong coupling between B and T_1 exists, the coefficient of variation is larger for T_2 than for T_1, namely 0.16 vs. 0.08. Relatively more can be gained from improving T_2 estimation than T_1 estimation. A possibility would be to reevaluate the settings for the spin echo prepared images. It should be evaluated what the gain is in reproducibility in T_2 when more SE prepared images are acquired or when the used T_E range is increased.

6

Conclusion

This thesis was set out to explore the reproducibility of T_1 and T_2, where an optimized acquisition scheme was used. The challenges posed in T_1 and T_2 mapping by this acquisition scheme were evaluated, where we looked at image registration and parameter estimation using complex data.

We conclude that the reproducibility of T_1 and T_2 with our proposed method is sufficient to potentially allow the characterization of several plaque components in patient studies. Our patient example showed the presence of different T_1 and T_2 regions in the plaque. For further analysis of the quantification of plaque components using T_1 and T_2, more patients need to be scanned.

The reproducibility of our proposed method suffers from a few limitations, e.g. the accurate estimation of B and the accuracy of the image registration. Future work, as was discussed in Section 5, could potentially resolve these limitations.

To my knowledge, no quantitative study has been performed to this day that evaluated the reproducibility of T_1 and T_2 estimation of the carotid artery wall using a spin echo based 3D imaging protocol. Results are comparable with the carotid T_1 and T_2 estimated by Coolen et al. [15] where a variable flip angle approach was employed. The experiments performed in this thesis show promising initial results regarding tissue quantification using T_1 and T_2 of carotid atherosclerotic plaque.

Appendix A

Literature review

Stroke and atherosclerotic plaque

Strokes are the cause of roughly 140.000 deaths annually in the US [1]. 87% of these strokes are caused by an ischemic event [2] where carotid atherosclerotic plaque rupture contributes to 15-20% of all ischemic strokes [3]. Carotid atherosclerotic plaque is the result of an inflammation in the carotid vessel wall, which gets progressively worse [4, 5]. Vulnerable atherosclerotic plaque can rupture and its contents can form thrombotic material that is expelled in the artery. When this thrombotic material gets stuck in a narrow cerebral artery, an ischemic event results. The luminal narrowing caused by the growing of the plaque, called stenosis, has commonly been used for identification of plaque severity. This was already done in the 1980's on the coronary artery [45].

But there have been signs that plaque composition is also important in identification of plaque severity. Intraplaque hemorrhages (IPH) have shown to be a risk factor in plaque vulnerability. Carr et al. [46] and Ota et al. [47] showed that there was a strong correlation between IPH and plaque rupture. van den Bouwhuijsen et al. [8] found that a high load of calcification is often related to more hemorrhagic components in the plaque core. Mughal et al. [3] point out that cholesterol crystals in the lipid core can also cause IPH, by tearing apart the vasa vasorum of the intima which causes additional lipids, originating from the blood in the vasa vasorum, to enter the intima and enlarge the lipid core. Takaya et al. [9] also found that IPH stimulate

progression of atherosclerosis by increasing the lipid core and plaque volume. This additional material puts more strain on the thin cap that keeps the core material in place.

We can conclude that early diagnosis of vulnerable plaque and the specific contents of the plaque are of utmost importance. Using plaque composition analysis, the rupture risk of vulnerable plaque can be assessed.

Imaging modalities

There are several imaging modalities that are able to visualize plaque presence and plaque composition. X-ray angiography and intravascular ultrasound (IVUS), have excellent resolution and provide good information on the composition of plaque [48]. Limitations of the spatial resolution makes recognition of a thin fibrous cap impossible and possible altered gray values caused by display controls such as brightness and gain make IVUS incapable to accurately discriminate tissue components [49]. X-ray angiography has as disadvantage that it uses harmful radiation, both in imaging as in contrast agent. Both above described methods also have as disadvantage that they are invasive [50].

Non-invasive methods do suffer from lower resolution [49], but the non-invasiveness of these methods outweighs the disadvantages. Surface ultrasound, can indicate vessel thickening, but is unable to provide information on the cause of this thickening. Surface ultrasound measurements are also very observer dependent and suffer from low reproducibility [10]. CT and Magnetic Resonance Imaging (MRI) have the potential to be the most prominent imaging modalities for plaque detection. Both methods are able to characterize plaque composition [50]. As with angiography, a disadvantage of CT is the use of radiation in imaging. MRI suffers from possible motion artifacts, due to longer scan times than for CT imaging [49].

MRI can characterize plaque composition based on tissue properties [10, 11]. These tissue properties, called T_1 and T_2 are magnetic relaxation times, and are tissue specific. Quantification is performed by fitting a mathematical model to the data of images taken with different pulse sequence settings. These pulse sequence settings and the tissue T_1 and T_2 determine the signal intensity at the moment the image is acquired.

The quantification of T_1 and T_2 involves on one end, the acquisition of MR images and on the other end the estimation of T_1 and T_2. We will elaborate on two parts of this image processing, namely image registration and mapping.

Image registration

During the acquisition of the MR images, translation of the subject can occur due to breathing, swallowing or repositioning of the head. This results in a misalignment between all images and hampers quantitative assessment, since in this case a given voxel does not represent the same anatomical structure in each image. To account for these effects, image registration can be applied. In this section we will discuss two registration methods; pairwise registration and groupwise registration.

Pairwise registration

Pairwise registration involves the alignment of one fixed image and one moving image, and is the most conventional registration method. Guyader et al. [51] use pairwise registration as preprocessing step for quantification of diffusion tensors in diffusion weighted images of the abdomen. They also considered interpolations and Gaussian blurring as alternative strategies to compensate for motion between images. However, they concluded that image registration yields the best alignment between images.

Bron et al. [29] used automated registration to register T_1 weighted images of the femur and tibia, separately. The image of the femur, that showed the highest contrast was used as fixed image during the registration of the femoral images. A similar procedure was performed for the tibial images. Applying image registration before T_1 mapping significantly improved the 90% percentile of the CRLB.

Pairwise registration is also used in the alignment of carotid images. Van 't Klooster et al. [28], validated the use of automatic grid-based image registration of the carotid artery. They tested various mask sizes similarity metrics and gridsizes. Similarity metrics give a measure of the similarity between images. In registration, this metric is maximized to increase the similarity between moving and fixed images. Several metrics are based on gradients in the image, correlation or mutual information between images [52]. They conclude that the most optimal registration involves a non-rigid

transformation, with a gridsize of 16mm and a metric based on mutual information.

Groupwise registration

In groupwise registration, multiple images are registered in one optimization. By registering multiple images in one registration, the optimization process utilizes the information of all images and is thus less sensitive to outliers [53]. A drawback of groupwise registration is the increase in dimensionality due to an increased number of samples being used in the optimization [53], which could make the optimization process more cumbersome and slower.

Metz et al. [54] propose a groupwise method for dynamic medical imaging data, which takes smoothness into account in both spatial and temporal directions of the data. Their method was tested on imaging data of the heart and the lung. They showed that groupwise registration performed better than a registration method that uses reference time point, regarding consistency of the results.

Huizinga et al. [27] propose a metric that involves Principal Component Analysis (PCA) of the correlation matrix, which is insensitive to intensity scaling of the images, whereas PCA of the covariance matrix suffers from this disadvantage. The dissimilarity metric promotes that as much variance as possible is explained by a few large eigenvalues. Results show that groupwise registration with a PCA based metric gives a lower CRLB than pairwise registration methods, and other groupwise registration methods based on sum of variances [54], or sum of the squared elements of the correlation matrix [55]. It PCA based groupwise registration also shows a lower CRLB than methods based on mutual information [56] and methods based on the residual error of the signal model fit [57].

Mapping

The signal that is acquired during an MRI scan does not fill the spatial domain of an image, but rather the frequency domain, called k-space. The signals that fill these k-space lines are complex valued. They consist of superimposed cosine and sine functions, which have a real and imaginary part, together formed by the amplitude and the phase of the signal. For clinical diagnosis, the magnitude of the signal is used and the phase of the signal is discarded [58]. For quantification of tissue properties it might be useful

to retain the phase data of the signal. Already in the 1990's, Gowland and Leach [58] started using Phase Sensitive Inversion Recovery (PSIR), where the sign of the magnitude data was restored by evaluating the phase images.

In the next subsections we will elaborate on T_1 and T_2 quantification that has been done with magnitude data, polarity restored magnitude data and complex data in other research. Polarity restored magnitude data consists of, as the name suggests, restoring the polarity, or sign, of the longitudinal magnetization by evaluating the difference in phase between subsequent images. A 180 degree difference in phase indicates that the magnetization has changed sign between the acquisition of these images. Intrinsically, MR data is complex in nature. Quantification with complex data utilizes both the real and imaginary parts of the signal to which a mathematical model is fitted.

T_1 mapping

Magnitude

There are several groups that use magnitude data for T_1 estimation in carotid plaques. Fanea et al. [20] used five magnitude images (256x128 pixels) where an inversion recovery (IR) sequence was used to estimate T_1 of a hardware phantom. IR is a pulse sequence that induces a T_1 weighting of an image [16] and only induces a change in longitudinal magnetization M_z. Fanea et al. [20] evaluated two methods to estimate T_1. In the first method they directly fitted a signal model to the set of acquired T_1 weighted magnitude images. For the second method they acquired one T_1 weighted image and one proton density image. By computing the ratio between the signal intensity in the proton density image and T_1 weighted image, they estimated T_1. They concluded that the last method, utilizing only two images to estimate T_1, was clinically more feasible, due to lower computation times of T_1. However, they concluded that this method was less robust for exact T_1 estimation than the first method.

Coolen et al. [14, 15] use a variable flip angle (VFA) approach for T_1 estimation of the carotid. In this approach, the magnetization of the spins is repeatedly perturbed by an RF pulse of duration t which results in a α degrees flip of the magnetization, inducing a T_1 weighted effect in the image. In between each perturbation an image is acquired. Coolen et al. [14, 15] assume exact knowledge of the flip angle used in acquisition of the images. However, due to local magnetic field inhomogeneities, the flip angle that is

introduced to the patient can be incorrect. This could potentially lead to incorrect estimation of T_1.

Polarity restored and complex data

There are many researchers that opt for polarity restored magnitude data for estimating T_1 [23, 26, 58–63]. Research topics that use this method vary from cartilage T_1 estimation [59], to myocardial T_1 mapping [23, 62, 63] and arterial T_1 mapping [60, 61]. In the 1990's, Gowland and Leach [58] started the development of phase sensitive inversion recovery (PSIR), in which the polarity of the data is recovered by evaluating the phase of the signal. Reference images were used to correct for phase changes in subsequently acquired images. By subtracting the phase image from the reference phase image, polarity change can be determined. A 180 degree change in phase indicates a change in signal sign. The use of polarity restored magnitude data can contribute to a more accurate estimation of T_1 than using magnitude data. Using magnitude data could result in ambiguity in estimation; see Section 2.4.1.

Another application of PSIR involves the enhancement of image contrast. Kellman et al. [62] have showed that the contrast between two tissues can be enhanced when PSIR is used. We can illustrate this with Figure A.1. The magnitude magnetic relaxation curves of two tissues are given by the blue and ochre curve. When we take a measurement at $t = 230ms$, there would be almost no difference in signal intensity between both tissues. If the polarity restored data is used, the red curve instead of the blue curve, a signal difference of 0.2 between tissue 1 and 2, would be present at this measurement point. The contrast would increase when the polarity restored data is used, compared to the contrast between the tissues in the magnitude images. This holds, if a T_I is chosen that lies between the null times of both tissues. Kellman et al. also found that T_1 estimation, using polarity restored data is less sensitive to uncertainty in T_I. An uncertainty in T_I could potentially change the polarity of the magnetization at a point around the null time. Therefore, if the polarity of the signal at that point is assumed incorrect, the estimated T_1 is potentially incorrect. Kellman et al. [63] state that the use of PSIR improves the precision of the estimation of T_1 in regions where tissue null times are close to the used T_I with 30%, compared to T_1 estimation using magnitude data.

A problem with (polarity restored) magnitude data is the fact that the

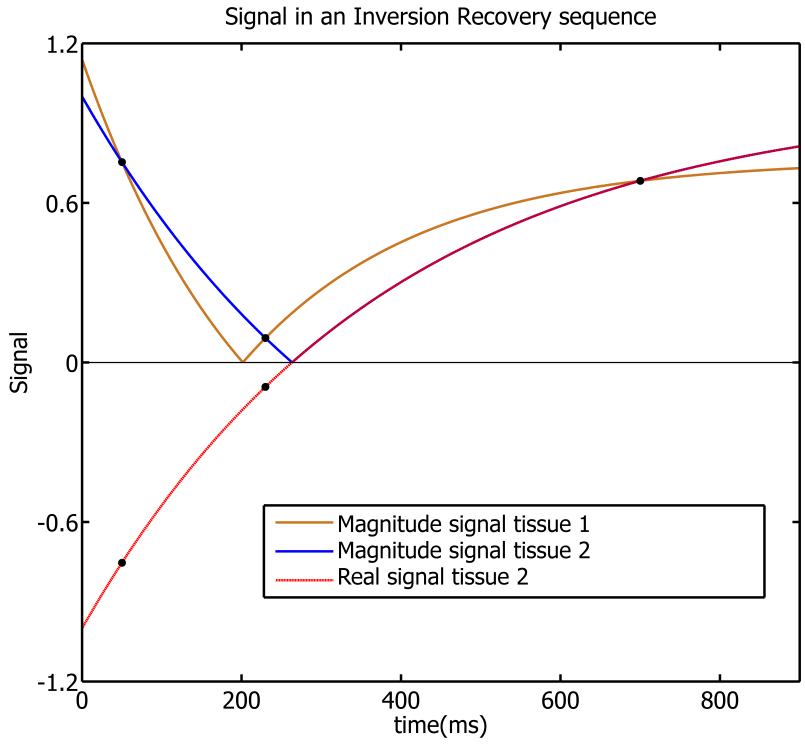

Figure A.1: Magnitude signal for tissue 1 (ochre) and real and magnitude signal for tissue 2 (red and blue)

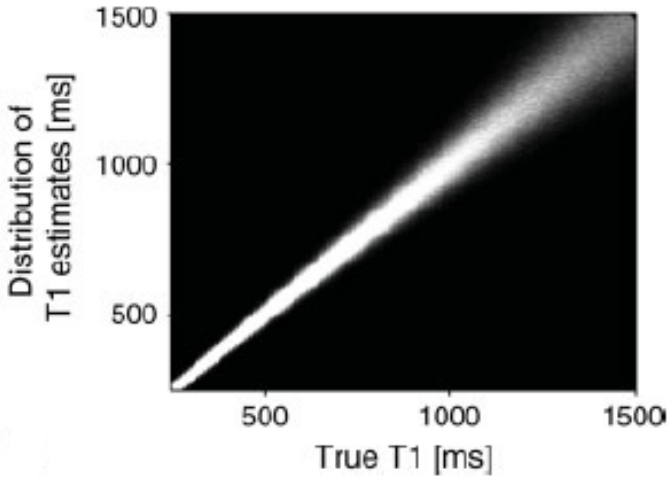

Figure A.2: T_1 estimates as a function of true T_1 [19]

data is Rician distributed. The noise of the complex data consists of a zero mean Gaussian distribution with a standard deviation σ on both the real and imaginary axis. For the magnitude data this 2D Gaussian distribution translates to the Rician distribution [64]. This distribution is centered at a value μ which is always greater than zero. Parameter estimation for low SNR (<2) can therefore be biased, and yield inaccurate results [65]. Barral et al. [19] evaluated the use of polarity restored magnitude data and complex data, regarding T_1 precision. They tested the precision for a range of SNR and as in previous cases they used an IR sequence. Their methods were tested on simulated data as well as on hardware phantom and volunteer data. In their approach they go more in depth in the fitting of the acquired data.

Barral et al. [19] found that T_1 estimation using polarity restored data performed worse than estimation based on complex data. They evaluated the root mean square error (RMSE) for a range of noise standard deviations. At low SNR, and thus large noise standard deviation (σ_n>0.05), the parameters estimated with the complex data and complex signal model represented the data better than the parameters estimated using polarity restored data and the magnitude model. At high SNR (σ_n<0.05) both methods perform equally as good. Barral et al. estimated the relation between the precision of T_1 estimation as a function of true T_1 (Figure A.2). For increasing true T_1, there is a larger spread in T_1 estimates than for low T_1 values. They have not tested their methods on T_2 estimation.

T_2 mapping

The use of complex data has no direct effect, due to loss of signal polarity, on the estimation on T_2. There is potentially an effect on the estimation due to the distribution of the data. As discussed before, when the magnitude signal is used for T_2 estimation a bias in results may occur, due to a Rician distribution of the data [24, 25]. For lower SNR regions the bias increases, and the estimation for T_2 can potentially be incorrect [25]. Using the complex data, averts the possible bias due to a Rician distribution of the data.

There are several factors that need to be taken care of when using complex data. The introduction of the phase in the parameter estimation brings additional uncertainty to the fitting. Phase errors can limit the applicability of PSIR and full complex IR methods. Sources of phase errors include non-centering of the echo in the readout window, variations in patient loading, coil sensitivity and phase shifts from bandwidth filters [26].

Estimation improvement

As was discussed in the last subsection there are many options to perform image registration, using different metrics or different transformations. Pairwise registration is the most basic form of image registration, taking one fixed and one moving image. This however introduces a bias, due to the choice of reference image that is taken. A groupwise registration method is more robust, using more images in one optimization, making the end result less sensitive to outliers.

The methods discussed on mapping all have the same goal; to accurately estimate the T_1 and T_2 for plaque identification. The use of magnitude data is sufficient for T_1 and T_2 weighted imaging. For accurate quantification of T_1 and T_2 this is not enough. Using magnitude data is computationally less intensive than the use of complex data, since two dimensional data is reduced to only a single dimension. But this method is less robust for T_1 and T_2 estimation when the signal noise is higher, due to the Rician distribution of the data. The gain in additional information as well as the unbiased 2D Gaussian noise of complex data, seems to be more beneficial in parameter estimations than using magnitude data.

From the work of Faena et al. [20] we can conclude that using magnitude data, requires more images for robust T_1 estimation. This is due to the am-

biguity in T_1 estimation, as explained in Figure 13. Acquiring more images is disadvantageous for patients. Due to a longer stay in the MRI machine, more movement by the patient can be expected, and thus more artifacts and inaccuracies in T_1 mapping is expected.

As was pointed out, the quality of the estimations is less when polarity restored magnitude data is used than when complex data is used. With polarity restored magnitude data, the same bias problem occurs, due to the Rician character of the data. The use of complex data in the quantification of T_1 and T_2 in carotid atherosclerotic plaque can potentially contribute to robust characterization of plaque components, which may eventually be a better indicator for plaque rupture risk than the currently used luminal stenosis.

Appendix B

ISMRM Abstract: Resolving ambiguity in T_1 mapping using complex MRI data

Kees M. van Hespen[1], Dirk H.J. Poot[1,2], Harm A. Nieuwstadt[1], and Stefan Klein[1]

[1]Departments of Medical Informatics and Radiology, Erasmus MC, Rotterdam, Netherlands, [2]Imaging Science and Technology, Delft University of Technology, Delft, Netherlands

Synopsis

We have recently developed an optimized T_1 mapping protocol for carotid atherosclerotic plaque imaging, using a combination of inversion and recovery prepared acquisitions. This protocol requires less images to be taken (and thus shorter acquisition time) for precise T_1 estimation than conventional inversion or saturation-prepared acquisition schemes. However, estimating T_1 from magnitude data, acquired with the optimized settings, causes bimodality of T_1 estimates, due to the ambiguity in sign of the inversion prepared magnitude images. Simulations and experiments on a hardware phantom and a volunteer show that the ambiguity resolves

when we fit a complex-valued model to the complex data.

Purpose

Rupture of carotid atherosclerotic plaque is a major cause of stroke. Plaque composition, is believed to be an important indicator for rupture risk. For quantitative assessment of plaque composition, T_1 and T_2 relaxation times can be used[1]. In general, T_1 can be accurately and efficiently quantified by a combined set of inversion and/or saturation prepared fast spin echo (FSE) acquisitions[2]. Our aim is to apply such a technique for T_1 mapping in the carotid artery wall. Conventionally, the T_1 is estimated by fitting a signal model to the acquired magnitude images. However, the removal of the sign information by only considering the magnitude data of inversion prepared images, can lead to ambiguous T_1 values when the number of images is low (see Figure B.1). In this study, we investigate if ambiguity in T_1 estimation can be eliminated by fitting complex-valued data.

Methods

We focus on T_1 mapping based on a set of inversion and saturation prepared acquisitions. The magnitude signal model is as follows:

Model 1: $S = |A(1 - Be^{-T_I R_1} + (B-1)e^{-R_1 T_R})|$

where B is the inversion efficiency, T_I the inversion time, T_R the repetition time, R_1 the relaxation rate and A the unprepared magnitude. The complex signal model is given by:

Model 2: $S = r_a e^{i\phi_a}(1 - Be^{-T_I R_1} + (B-1)e^{-R_1 T_R})$

with r_a the unprepared magnitude, and ϕ_a the phase of the signal.

For readout, we use a stabilized 3D FSE acquisition[3], which leads to black blood imaging suitable for carotid wall analysis. The preparation in each acquisition consists of the saturation by the preceding readout, possibly followed by an inversion pulse. Parameters T_I and T_R were optimized numerically, so as to maximize the time efficiency of the entire protocol, resulting in: T_I/T_R = 91/973, 429/3725, -/1074, -/907ms. From this set of four inversion/saturation prepared images we estimate T_1 by either a) fitting

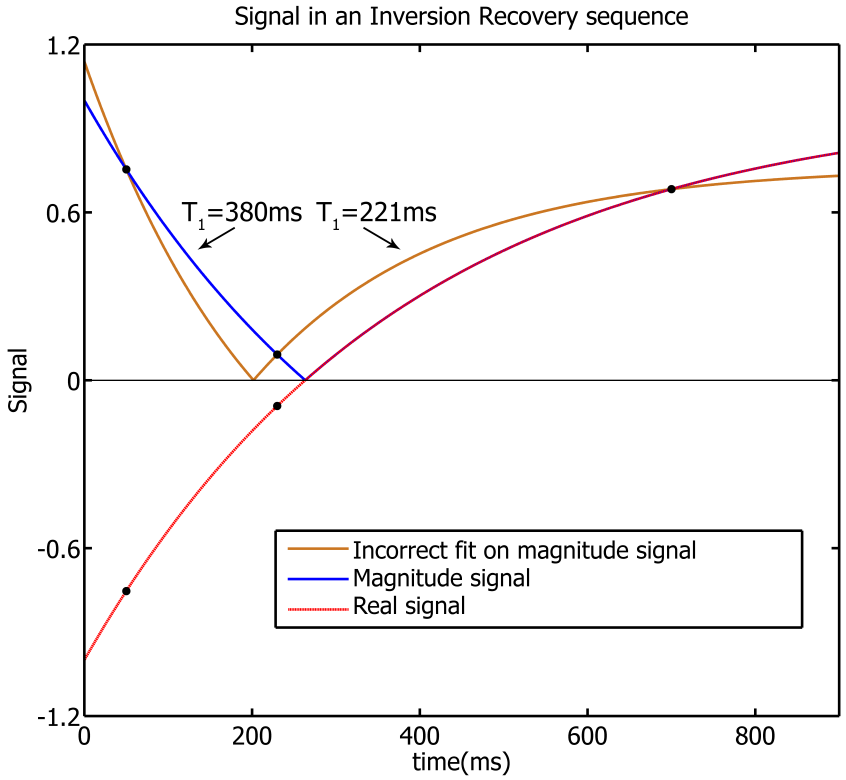

Figure B.1: Ambiguity in fitting the magnitude of the signal (Red), yielding two possible solutions T_1=380ms (Blue, correct solution) and T_1=221ms (Ochre, incorrect solution)

Model 1 to the magnitude data, or b) fitting Model 2 to the complex-valued data. Fitting was done with a maximum likelihood estimation approach[4].

In a Monte Carlo simulation, data was generated using the complex signal model and the optimized parameters, for a range of T_1 values (100 through 1500ms) occurring in carotid plaque, $B = 1.9$, $r_a = 1000$, ϕ_a=0, and Gaussian noise, μ=0 and σ=33, was added to the real and imaginary parts for each of 10.000 independent realizations.

In a hardware phantom experiment, 12 tubes were filled with water and different concentrations of gadolinium trichloride to reduce T_1 and agarose to reduce T_2[1]. For our imaging protocol we used an echo-train-length of 18, echo spacing of 6ms and an acquired voxel-size of 0.625x0.71x2mm^3.

In an *in vivo* example, a healthy volunteer is scanned with the aforementioned protocol and parameters.

Results

Figure B.2 shows the distribution of estimated T_1 for the Monte Carlo experiment (true T_1=846ms). A bimodal distribution can be observed for the T_1 estimates when Model 1 is used. After setting a manual threshold to sort the estimates to one of the modes, we fit a normal distribution to each mode with a built-in function of Matlab (normfit). Using Model 1, the modes are T_1=854±47.6ms and 539±32.6ms. Using Model 2 results in a single mode: T_1=846.5±47.7ms. For the entire range of T_1 (See Figure B.3.A), a bimodal distribution is observed. Bimodality was assumed if the means of the assumed modes were more than two σ apart. When Model 2 is used, the ambiguity issue is resolved (Figure B.3.B) and the correct T_1 is recovered for all simulated T_1.

In the hardware phantom experiment, several tubes show a non-uniform, bimodal T_1 map (Figure B.4.A) when Model 1 is used. In the example tube, Figure B.4.B, two modes can observed: T_1=846.6±10.9ms and 541.5±8.7ms. Using Model 2 results in uniform T_1 maps in all tubes. The example tube (Figure B.4.D) shows a single mode: T_1=846.1±12.3ms, which corresponds to the T_1 found in the Monte Carlo experiment (Figure B.2).

The *in vivo* example (Figure B.5) shows that using Model 1 yields estimates T_1=510.61±289.41ms in the carotid wall. With Model 2, T_1 values of 939.12±206.75ms are found, which are in accordance with those found in previous studies (700-900ms)[1].

Discussion

Ambiguity in T_1 values estimated from magnitude data acquired with optimized T_I/T_R settings was resolved by using complex data. This benefit of using complex data for T_1 estimation has previously not been explicitly identified[5]. Our complex model enables us to use the optimized T_I/T_R settings, which require less scan time than conventional inversion recovery protocols that require more images for robust estimation. Hence, we conclude that T_1 mapping with optimized T_I/T_R settings is more robust when complex data is used for the fitting.

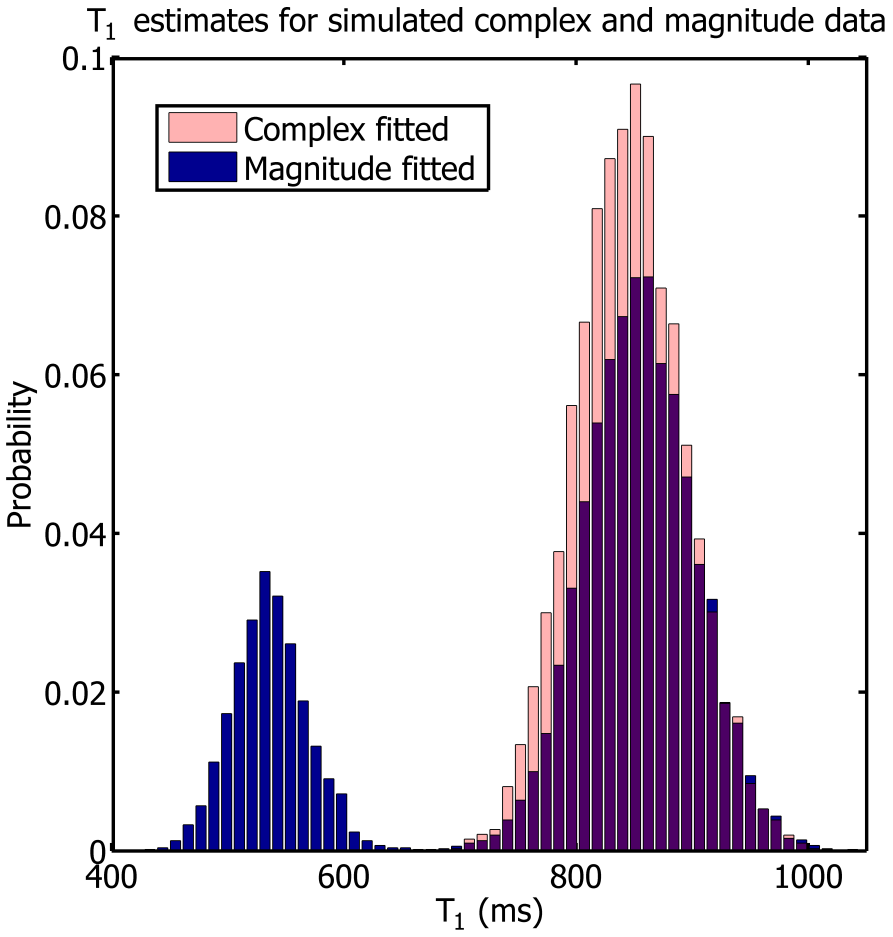

Figure B.2: Probability of finding an estimate T_1, using the magnitude (Blue) or complex model (Red), given a true T_1=846ms, B=1.9, Signal-to-noise ratio=30 and bin size=11

References

1. B. F. Coolen, D. H. Poot, M. I. Liem, L. P. Smits, S. Gao, G. Kotek, S. Klein, and A. J. Nederveen. Three-dimensional quantitative T1 and T2 mapping of the carotid artery: Sequence design and in vivo feasibility. Magn Reson Med, 2015.

2. N. Stikov, M. Boudreau, I. R. Levesque, C. L. Tardif, J. K. Barral, and G. B. Pike. On the accuracy of T1 mapping: searching for common ground. Magn Reson Med, 73(2):514-22, 2015.

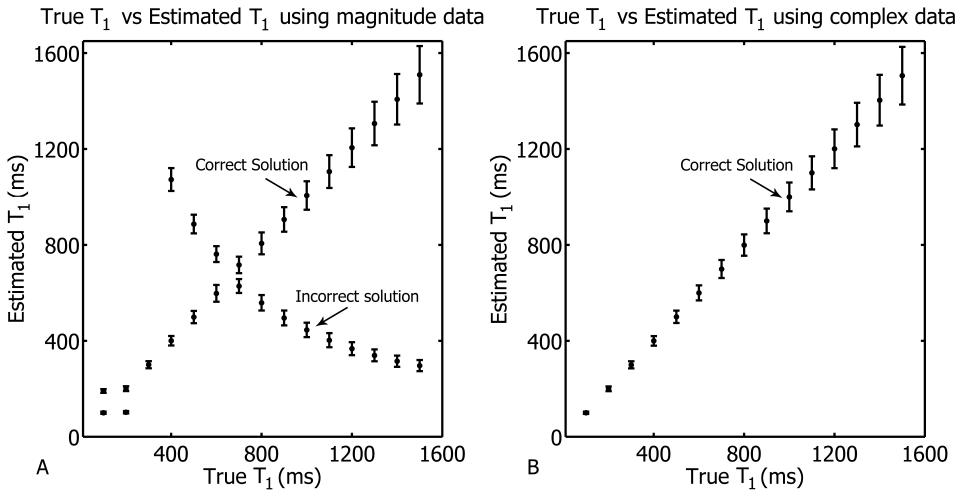

Figure B.3: Estimated T_1 in our Monte Carlo experiment for magnitude (A) and complex (B) data. Yielding incorrect solutions as well as correct solutions when magnitude data is used

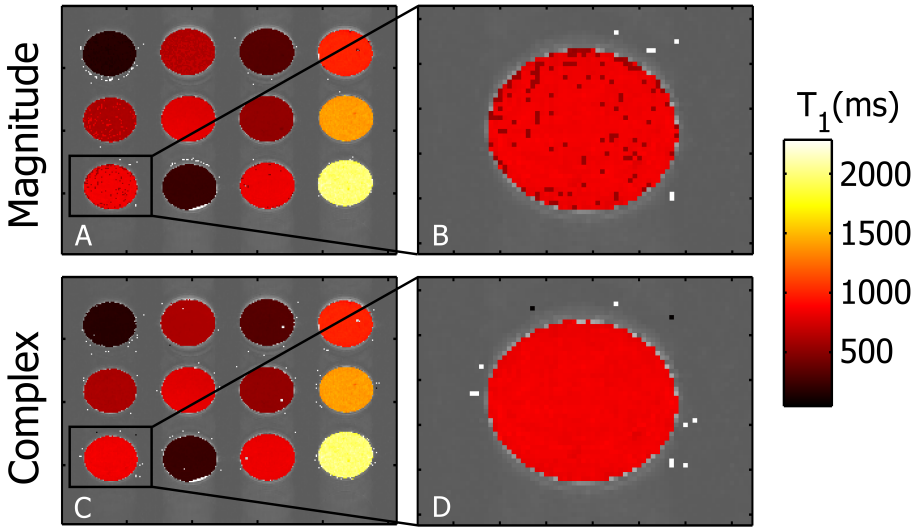

Figure B.4: Hardware phantom T_1 mapping using the magnitude (A,B) and complex (C,D) model

3. R. F. Busse, H. Hariharan, A. Vu, and J. H. Brittain. Fast spin echo sequences with very long echo trains: design of variable refocusing flip angle schedules and generation of clinical T2 contrast. Magn Reson Med, 55(5):1030-7, 2006.

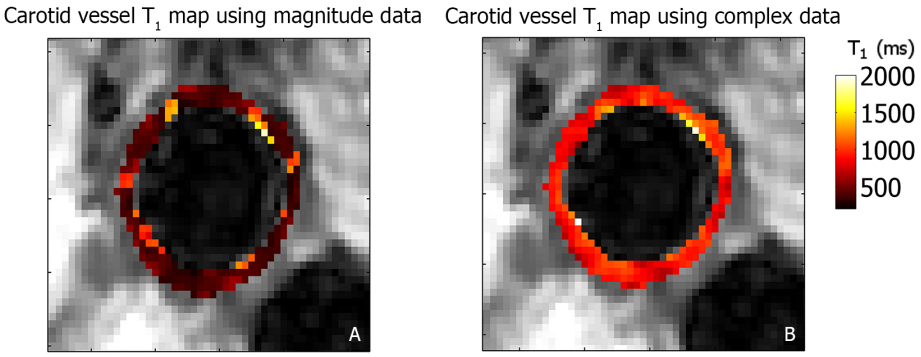

Figure B.5: T_1 mapping of the carotid artery wall using the magnitude (A) and complex (B) model. Yielding an estimated T_1=510.61±289.41ms and 939.12±206.75ms, using the magnitude and complex model respectively

4. D. H. Poot, and S. Klein. Detecting Statistically Significant Differences in Quantitative MRI Experiments, Applied to Diffusion Tensor Imaging. IEEE Transactions on Medical Imaging, 34(5): 1164-1176, 2015.

5. J. K. Barral, E. Gudmundson, N. Stikov, M. Etezadi-Amoli, P. Stoica, and D. G. Nishimura. A robust methodology for in vivo T1 mapping. Magn Reson Med, 64(4):1057-67, 2010.

Appendix C

Experiment: Optimal constant B

In initial experiments using scenario 1, we chose $B = 1.95$ as a constant. This value may not actually correspond to the actual B of the spins in the tissue. We evaluated the residual images, $R_g(x) = S_g(x) - \hat{S}_g(x)$ where $\hat{S}_g(x)$ is the estimated signal for image g, for a range of B to test the validity of $B = 1.95$. In this experiment, the influence of B on the residual was evaluated using volunteer data.

C.1 Methods

The evaluation of the residual was performed on scan 1 and scan 2 of volunteer 31, using a range of B from 1.70 to 2.00, with increments of 0.01. A measure of standard deviation is used to evaluate the residual images. This measure is given by:

$$\sigma = \frac{1}{G\ P}\sqrt{\frac{\sum_{g=1}^{G}\sum_{x=1}^{N} R_g(x)\ R_g(x)^*}{2\ G-P}} \tag{23}$$

Where $R_g(x)$, is the residual of voxel x in image g. G is the number of images, and P the number of estimated parameters.

Two masks were used; the first one is drawn outside the carotid in a homogeneous area in a few slices (780 voxels), see Figure C.1. The second

mask is the carotid mask (865 voxels) used in the evaluation of T_1 and T_2 in other experiments, described in Section 3.3.

C.2 Results

In Figures C.2 and C.3, σ is given as a function of B for the first mask on scan 1 and scan 2. σ is minimal for scan 1 around $B = 1.81$ and around $B = 1.78$ for scan 2. Compared to $B = 1.95$, σ decreases 6 and 15% when the optimal B is used for scan 1 and scan 2, respectively.

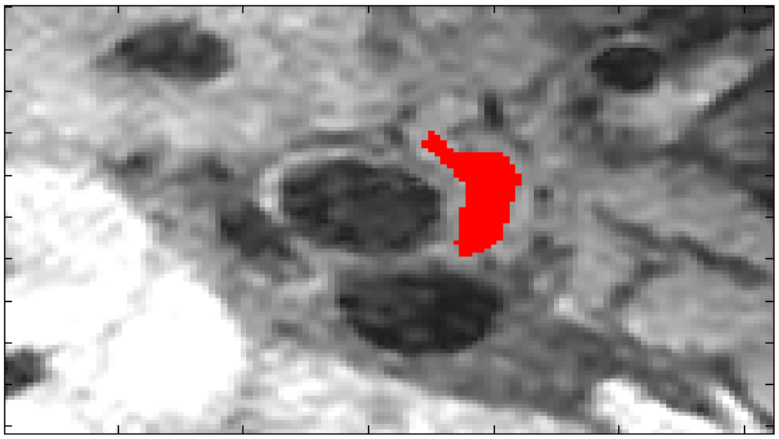

Figure C.1: Mask outside the carotid wall given in red

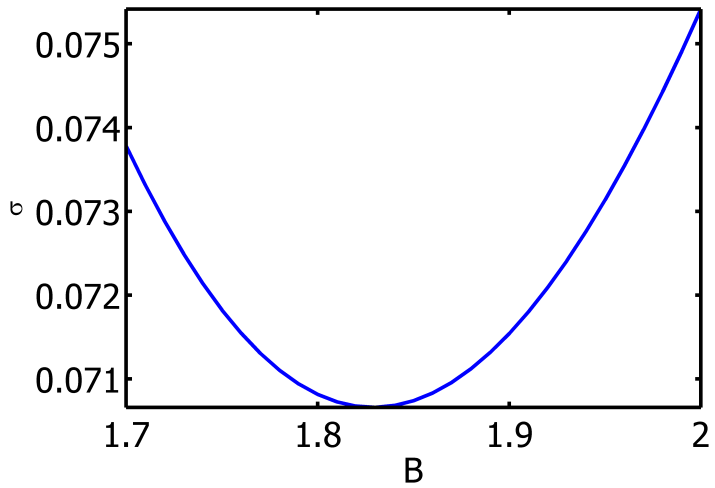

Figure C.2: Scan 1: σ as a function of B, using a mask outside the carotid wall

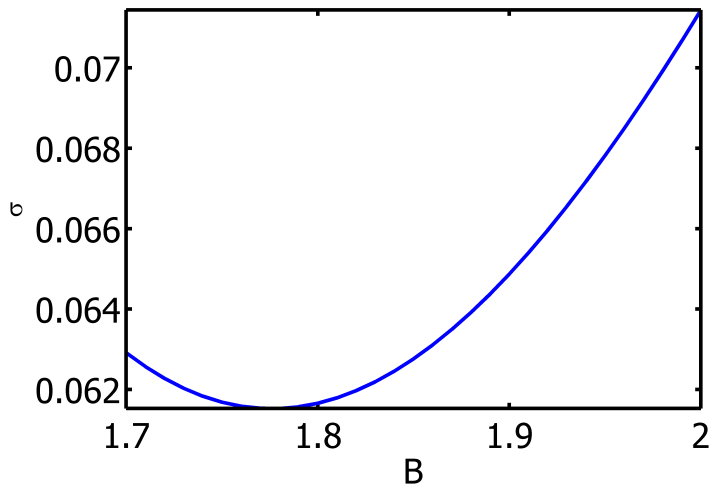

Figure C.3: Scan 2: σ as a function of B, using a mask outside the carotid wall

Using the carotid mask, the results are slightly different (Figures C.4 and C.5). The minimum σ for scan 1 is located at $B = 1.69$. For scan 2 we observe a minimal σ at $B = 1.72$. There is a difference in B of up to 0.1, given the minimum in σ, between a mask drawn at the carotid wall and a mask drawn outside the carotid.

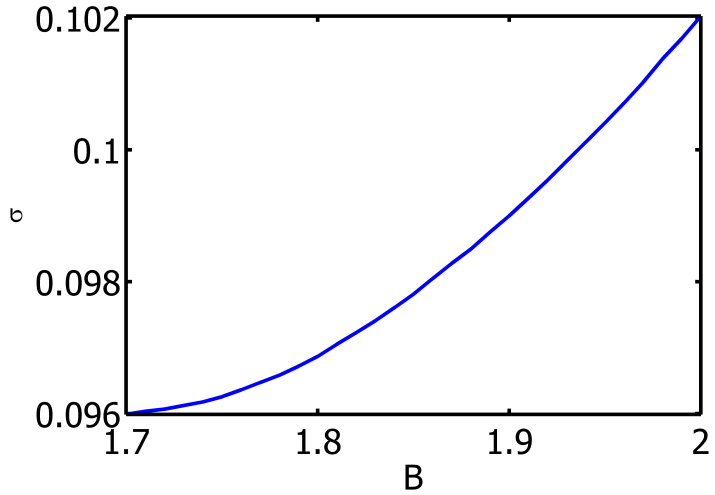

Figure C.4: Scan 1: σ as a function of B, using the carotid mask

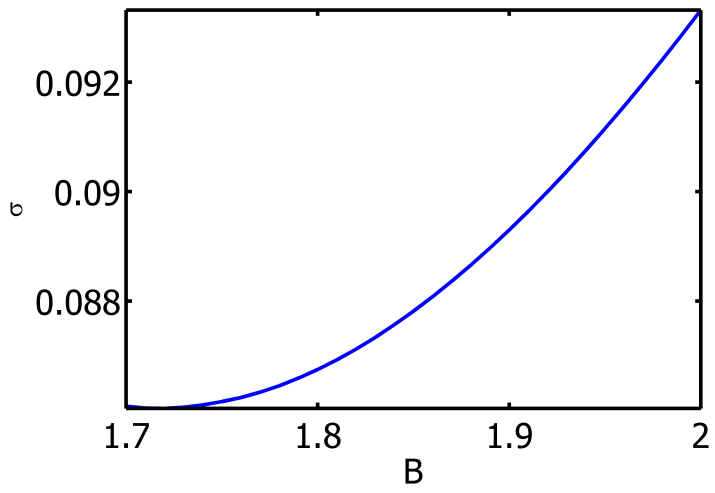

Figure C.5: Scan 2: σ as a function of B, using the carotid mask

C.3 Conclusion

We can conclude that for different anatomical structures, the optimal B, that minimizes the residual, varies for each structure. The difference in optimal B between these structures can become as large as 0.1, even though these structures are located next to each other. This leads us to believe that we should not try to fit a single B to the ROI, but estimate B. Using regularization we can influence the spatial variability of the voxelwise estimated B, and allow it to vary according to expected values.

Bibliography

1. D. Lloyd-Jones, R. J. Adams, T. M. Brown, M. Carnethon, S. Dai, G. De Simone, T. B. Ferguson, E. Ford, K. Furie, C. Gillespie, A. Go, K. Greenlund, N. Haase, S. Hailpern, P. M. Ho, V. Howard, B. Kissela, S. Kittner, D. Lackland, L. Lisabeth, A. Marelli, M. M. McDermott, J. Meigs, D. Mozaffarian, M. Mussolino, G. Nichol, V. L. Roger, W. Rosamond, R. Sacco, P. Sorlie, R. Stafford, T. Thom, S. Wasserthiel-Smoller, N. D. Wong, J. Wylie-Rosett, Committee American Heart Association Statistics, and Subcommittee Stroke Statistics. Executive summary: heart disease and stroke statistics–2010 update: a report from the American Heart Association. *Circulation*, 121(7):948–54, 2010.

2. Ischemic Strokes (Clots). <http://www.strokeassociation.org/STROKEORG/AboutStroke/TypesofStroke/IschemicClots/Ischemic-Strokes-Clots_UCM_310939_Article.jsp>, 2015. [Last accessed: 11-09-2015].

3. M. M. Mughal, M. K. Khan, J. K. DeMarco, A. Majid, F. Shamoun, and G. S. Abela. Symptomatic and asymptomatic carotid artery plaque. *Expert Rev Cardiovasc Ther*, 9(10):1315–30, 2011.

4. P. Libby. Inflammation in atherosclerosis. *Arterioscler Thromb Vasc Biol*, 32(9):2045–51, 2012.

5. P. Libby. Atherosclerosis: the new view. *Sci Am*, 286(5):46–55, 2002.

6. P. J. Gagne, J. Matchett, D. MacFarland, M. Hauer-Jensen, G. W. Barone, J. F. Eidt, and R. W. Barnes. Can the NASCET technique for measuring carotid stenosis be reliably applied outside the trial? *J Vasc Surg*, 24(3):449–55; discussion 455–6, 1996.

7. X. Zhao, H. R. Underhill, Q. Zhao, J. Cai, F. Li, M. Oikawa, L. Dong, H. Ota, T. S. Hatsukami, B. Chu, and C. Yuan. Discriminating carotid atherosclerotic lesion severity by luminal stenosis and plaque burden: a comparison utilizing high-resolution magnetic resonance imaging at 3.0 Tesla. *Stroke*, 42(2):347–53, 2011.

8. Q. J. van den Bouwhuijsen, D. Bos, M. A. Ikram, A. Hofman, G. P. Krestin, O. H. Franco, A. van der Lugt, and M. W. Vernooij. Coexistence of Calcification, Intraplaque Hemorrhage and Lipid Core within the Asymptomatic Atherosclerotic Carotid Plaque: The Rotterdam Study. *Cerebrovasc Dis*, 39(5-6):319–24, 2015.

9. N. Takaya, C. Yuan, B. Chu, T. Saam, N. L. Polissar, G. P. Jarvik, C. Isaac, J. McDonough, C. Natiello, R. Small, M. S. Ferguson, and T. S. Hatsukami. Presence of intraplaque hemorrhage stimulates progression of carotid atherosclerotic plaques: a high-resolution magnetic resonance imaging study. *Circulation*, 111(21):2768–75, 2005.

10. B. M. Wallis de Vries, G. M. van Dam, R. A. Tio, J. L. Hillebrands, R. H. Slart, and C. J. Zeebregts. Current imaging modalities to visualize vulnerability within the atherosclerotic carotid plaque. *J Vasc Surg*, 48(6):1620–9, 2008.

11. J. F. Toussaint, G. M. LaMuraglia, J. F. Southern, V. Fuster, and H. L. Kantor. Magnetic resonance images lipid, fibrous, calcified, hemorrhagic, and thrombotic components of human atherosclerosis in vivo. *Circulation*, 94(5):932–8, 1996.

12. W. J. Rogers, J. W. Prichard, Y. L. Hu, P. R. Olson, D. H. Benckart, C. M. Kramer, D. A. Vido, and N. Reichek. Characterization of signal properties in atherosclerotic plaque components by intravascular MRI. *Arteriosclerosis Thrombosis and Vascular Biology*, 20(7):1824–1830, 2000.

13. L. Biasiolli, A. C. Lindsay, J. T. Chai, R. P. Choudhury, and M. D. Robson. In-vivo quantitative T-2 mapping of carotid arteries in atherosclerotic patients: segmentation and T-2 measurement of plaque components. *Journal of Cardiovascular Magnetic Resonance*, 15, 2013.

14. B. F. Coolen, D. H. Poot, M. I. Liem, L. P. Smits, S. Gao, G. Kotek, S. Klein, and A. J. Nederveen. Three-dimensional quantitative T1 and T2 mapping of the carotid artery: Sequence design and in vivo feasibility. *Magn Reson Med*, 2015.

15. B. A. Coolen, D.F. Heijtel, W.V. Potters, and A.J. Nederveen. 3D carotid wall T1 quantification using variable flip angle 3D Merge with steady-state recovery. *Proc. Intl. Soc. Mag. Reson. Med.*, 21, 2013.

16. N. Stikov, M. Boudreau, I. R. Levesque, C. L. Tardif, J. K. Barral, and G. B. Pike. On the accuracy of T1 mapping: searching for common ground. *Magn Reson Med*, 73(2):514–22, 2015.

17. J. P. Mugler. Optimized three-dimensional fast-spin-echo MRI. *J Magn Reson Imaging*, 39(4):745–67, 2014.

18. D. H. Poot and S. Klein. Detecting statistically significant differences in quantitative MRI experiments, applied to diffusion tensor imaging. *IEEE Trans Med Imaging*, 34(5):1164–76, 2015.

19. J. K. Barral, E. Gudmundson, N. Stikov, M. Etezadi-Amoli, P. Stoica, and D. G. Nishimura. A robust methodology for in vivo T1 mapping. *Magn Reson Med*, 64(4):1057–67, 2010.

20. L. Fanea and S. A. Sfrangeu. Relaxation Times Mapping Using Magnetic Resonance Imaging. *Romanian Reports in Physics*, 63(2):456–464, 2011.

21. H. Xue, S. Shah, A. Greiser, C. Guetter, A. Littmann, M. P. Jolly, A. E. Arai, S. Zuehlsdorff, J. Guehring, and P. Kellman. Motion correction for myocardial T1 mapping using image registration with synthetic image estimation. *Magn Reson Med*, 67(6):1644–55, 2012.

22. D. R. Messroghli, A. Radjenovic, S. Kozerke, D. M. Higgins, M. U. Sivananthan, and J. P. Ridgway. Modified Look-Locker inversion recovery (MOLLI) for high-resolution T1 mapping of the heart. *Magn Reson Med*, 52(1):141–6, 2004.

23. H. Xue, A. Greiser, S. Zuehlsdorff, M. P. Jolly, J. Guehring, A. E. Arai, and P. Kellman. Phase-sensitive inversion recovery for myocardial T1 mapping with motion correction and parametric fitting. *Magn Reson Med*, 69(5):1408–20, 2013.

24. R. D. Nowak. Wavelet-based Rician noise removal for magnetic resonance imaging. *IEEE Trans Image Process*, 8(10):1408–19, 1999.

25. J. V. Manjon, J. Carbonell-Caballero, J. J. Lull, G. Garcia-Marti, L. Marti-Bonmati, and M. Robles. MRI denoising using non-local means. *Med Image Anal*, 12(4):514–23, 2008.

26. P. Hou, K. M. Hasan, C. W. Sitton, J. S. Wolinsky, and P. A. Narayana. Phase-sensitive T1 inversion recovery imaging: a time-efficient interleaved technique for improved tissue contrast in neuroimaging. *AJNR Am J Neuroradiol*, 26(6):1432–8, 2005.

27. W. Huizinga, D. H. Poot, J. M. Guyader, R. Klaassen, B. F. Coolen, M. van Kranenburg, R. J. van Geuns, A. Uitterdijk, M. Polfliet, J. Vandemeulebroucke, A. Leemans, W. J. Niessen, and S. Klein. PCA-based groupwise image registration for quantitative MRI. *Med Image Anal*, 29:65–78, 2016.

28. R. van 't Klooster, M. Staring, S. Klein, R. M. Kwee, M. E. Kooi, J. H. Reiber, B. P. Lelieveldt, and R. J. van der Geest. Automated registration

of multispectral MR vessel wall images of the carotid artery. *Med Phys*, 40(12):121904, 2013.

29. E. E. Bron, J. van Tiel, H. Smit, D. H. Poot, W. J. Niessen, G. P. Krestin, H. Weinans, E. H. Oei, G. Kotek, and S. Klein. Image registration improves human knee cartilage T1 mapping with delayed gadolinium-enhanced MRI of cartilage (dGEMRIC). *Eur Radiol*, 23(1):246–52, 2013.

30. R. Busse. 3D FSE Reduces Scan Time, Generates Thinner slices. *Signa Pulse*, page 2, 2007.

31. J. Hennig, A. Nauerth, and H. Friedburg. RARE imaging: a fast imaging method for clinical MR. *Magn Reson Med*, 3(6):823–33, 1986.

32. J. Hornak. *The Basics of MRI*, volume 2005. 1996.

33. S. C. Deoni. High-resolution T1 mapping of the brain at 3T with driven equilibrium single pulse observation of T1 with high-speed incorporation of RF field inhomogeneities (DESPOT1-HIFI). *J Magn Reson Imaging*, 26(4):1106–11, 2007.

34. M. A.; Bernstein, K. F.; KIng, and X. J. Zhou. *Handbook of MRI pulse sequences*. Elsevier, San Diego, America, 2004.

35. S. Klein, M. Staring, K. Murphy, M. A. Viergever, and J. P. Pluim. elastix: a toolbox for intensity-based medical image registration. *IEEE Trans Med Imaging*, 29(1):196–205, 2010.

36. J. P. Pluim, J. B. Maintz, and M. A. Viergever. Mutual-information-based registration of medical images: a survey. *IEEE Trans Med Imaging*, 22(8):986–1004, 2003.

37. S. Klein, J. P. W. Pluim, M. Staring, and M. A. Viergever. Adaptive Stochastic Gradient Descent Optimisation for Image Registration. *International Journal of Computer Vision*, 81(3):227–239, 2008.

38. In Jae Myung. Tutorial on maximum likelihood estimation. *Journal of Mathematical Psychology*, 47(1):90–100, 2003.

39. A. T. Mai, F. Bastin, and M. Toulouse. On optimization algorithms for maximum likelihood estimation. 2014.

40. J. H. Halton. Algorithm 247: Radical-inverse quasi-random point sequence. *Commun. ACM*, 7(12):701–702, 1964.

41. R. D.; Dortch and M. D. Does. *Quantitative MRI in Cancer*. Imaging in medical diagnosis and therapy. Taylor and Francis, 2011.

42. F. Nielsen. Cramer-Rao Lower Bound and Information Geometry. *CoRR*, abs/1301.3578, 2013.

43. A. Brau. New parallel imaging method enhances imaging speed and accuracy. *GE Healthcare MR publication*, (Autumn 2007), 2007.

44. A. A. Harteveld, N. P. Denswil, J. C. Siero, J. J. Zwanenburg, A. Vink, B. Pouran, W. G. Spliet, D. W. Klomp, P. R. Luijten, M. J. Daemen, J. Hendrikse, and A. G. van der Kolk. Quantitative Intracranial Atherosclerotic Plaque Characterization at 7T MRI: An Ex Vivo Study with Histologic Validation. *AJNR Am J Neuroradiol*, 2015.

45. S. Glagov, E. Weisenberg, C. K. Zarins, R. Stankunavicius, and G. J. Kolettis. Compensatory enlargement of human atherosclerotic coronary arteries. *N Engl J Med*, 316(22):1371–5, 1987.

46. S. Carr, A. Farb, W. H. Pearce, R. Virmani, and J. S. Yao. Atherosclerotic plaque rupture in symptomatic carotid artery stenosis. *J Vasc Surg*, 23(5):755–65; discussion 765–6, 1996.

47. H. Ota, W. Yu, H. R. Underhill, M. Oikawa, L. Dong, X. Zhao, N. L. Polissar, B. Neradilek, T. Gao, Z. Zhang, Z. Yan, M. Guo, Z. Zhang, T. S. Hatsukami, and C. Yuan. Hemorrhage and large lipid-rich necrotic cores are independently associated with thin or ruptured fibrous caps: an in vivo 3T MRI study. *Arterioscler Thromb Vasc Biol*, 29(10):1696–701, 2009.

48. A. N. DeMaria, J. Narula, E. Mahmud, and S. Tsimikas. Imaging vulnerable plaque by ultrasound. *J Am Coll Cardiol*, 47(8 Suppl):C32–9, 2006.

49. D. Vancraeynest, A. Pasquet, V. Roelants, B. L. Gerber, and J. L. Vanoverschelde. Imaging the vulnerable plaque. *J Am Coll Cardiol*, 57(20):1961–79, 2011.

50. P. Schoenhagen, R. D. White, S. E. Nissen, and E. M. Tuzcu. Coronary imaging: angiography shows the stenosis, but IVUS, CT, and MRI show the plaque. *Cleve Clin J Med*, 70(8):713–9, 2003.

51. J. M. Guyader, L. Bernardin, N. H. Douglas, D. H. Poot, W. J. Niessen, and S. Klein. Influence of image registration on apparent diffusion coefficient images computed from free-breathing diffusion MR images of the abdomen. *J Magn Reson Imaging*, 42(2):315–30, 2015.

52. A. Gupta, H. K. Verma, and S. Gupta. Technology and research developments in carotid image registration. *Biomedical Signal Processing and Control*, 7(6):560–570, 2012.

53. K. A. Sidorov, S. Richmond, and D. Marshall. An Efficient Stochastic Approach to Groupwise Non-rigid Image Registration. *Cvpr: 2009 Ieee*

Conference on Computer Vision and Pattern Recognition, Vols 1-4, pages 2208–2213, 2009.

54. C. T. Metz, S. Klein, M. Schaap, T. van Walsum, and W. J. Niessen. Nonrigid registration of dynamic medical imaging data using nD + t B-splines and a groupwise optimization approach. *Med Image Anal*, 15(2):238–49, 2011.

55. C. Wachinger and N. Navab. Simultaneous registration of multiple images: similarity metrics and efficient optimization. *IEEE Trans Pattern Anal Mach Intell*, 35(5):1221–33, 2013.

56. K. K. Bhatia, J. Hajnal, A. Hammers, and D. Rueckert. Similarity metrics for groupwise non-rigid registration. *Med Image Comput Comput Assist Interv*, 10(Pt 2):544–52, 2007.

57. J. L. Andersson and S. Skare. A model-based method for retrospective correction of geometric distortions in diffusion-weighted EPI. *Neuroimage*, 16(1):177–99, 2002.

58. P. A. Gowland and M. O. Leach. A simple method for the restoration of signal polarity in multi-image inversion recovery sequences for measuring T1. *Magn Reson Med*, 18(1):224–31, 1991.

59. J. Szumowski, M. G. Durkan, E. W. Foss, D. S. Brown, E. Schwarz, and D. C. Crawford. Signal polarity restoration in a 3D inversion recovery sequence used with delayed gadolinium-enhanced magnetic resonance imaging of cartilage (dGEMRIC). *J Magn Reson Imaging*, 36(5):1248–55, 2012.

60. G. Bonanno, D. Brotman, and M. Stuber. Phase-sensitive dual-inversion recovery for accelerated carotid vessel wall imaging. *Invest Radiol*, 50(3):135–43, 2015.

61. K. Z. Abd-Elmoniem, R. G. Weiss, and M. Stuber. Phase-sensitive black-blood coronary vessel wall imaging. *Magn Reson Med*, 63(4):1021–30, 2010.

62. P. Kellman, A. E. Arai, E. R. McVeigh, and A. H. Aletras. Phase-sensitive inversion recovery for detecting myocardial infarction using gadolinium-delayed hyperenhancement. *Magn Reson Med*, 47(2):372–83, 2002.

63. P. Kellman and M. S. Hansen. T1-mapping in the heart: accuracy and precision. *J Cardiovasc Magn Reson*, 16:2, 2014.

64. A. J. den Dekker and J. Sijbers. Data distributions in magnetic resonance images: a review. *Phys Med*, 30(7):725–41, 2014.

65. H. Gudbjartsson and S. Patz. The Rician distribution of noisy MRI data. *Magn Reson Med*, 34(6):910–4, 1995.